Nano-Micro Letters

e-ISSN 2150-5551
CN 31-2103/TB

ARTICLE

https://doi.org/10.1007/s40820-025-01767-4

Cite as
Nano-Micro Lett.
(2025) 17:237

Received: 12 February 2025
Accepted: 9 April 2025

Se-Regulated MnS Porous Nanocubes Encapsulated in Carbon Nanofibers as High-Performance Anode for Sodium-Ion Batteries

Puwu Liang[1,2], Duo Pan[1], Xiang Hu[1] ✉, Ke R. Yang[5], Yangjie Liu[1], Zijing Huo[1,2], Zheng Bo[3], Lihong Xu[1], Junhua Xu[4] ✉, Zhenhai Wen[1] ✉

HIGHLIGHTS

- We have developed an efficient and scalable strategy to prepare a single-phase ternary $MnS_{0.5}Se_{0.5}$-carbon nanofiber composite with a defect-rich microstructure.
- The Na^+ storage mechanism of manganese-based sulfides after the incorporation of Se was thoroughly investigated, through systematic electrochemical characterization combined with theoretical calculations.
- The $MnS_{0.5}Se_{0.5}$@N-carbon nanofiber composite, used as an anode, exhibits excellent reversible capacity, rate capability, and cycling stability in sodium-ion batteries.

ABSTRACT Manganese-based chalcogenides have significant potential as anodes for sodium-ion batteries (SIBs) due to their high theoretical specific capacity, abundant natural reserves, and environmental friendliness. However, their application is hindered by poor cycling stability, resulting from severe volume changes during cycling and slow reaction kinetics due to their complex crystal structure. Here, an efficient and straightforward strategy was employed to in-situ encapsulate single-phase porous nanocubic $MnS_{0.5}Se_{0.5}$ into carbon nanofibers using electrospinning and the hard template method, thus forming a necklace-like porous $MnS_{0.5}Se_{0.5}$-carbon nanofiber composite ($MnS_{0.5}Se_{0.5}$@N-CNF). The introduction of Se significantly impacts both the composition and microstructure of $MnS_{0.5}Se_{0.5}$, including lattice distortion that generates additional defects, optimization of chemical bonds, and a nano-spatially confined design. In situ/ex-situ characterization and density functional theory calculations verified that this $MnS_{0.5}Se_{0.5}$@N-CNF alleviates the volume expansion and facilitates the transfer of Na^+/electron. As expected, $MnS_{0.5}Se_{0.5}$@N-CNF anode demonstrates excellent sodium storage performance, characterized by high initial Coulombic efficiency (90.8%), high-rate capability (370.5 mAh g^{-1} at 10 A g^{-1}) and long durability (over 5000 cycles at 5 A g^{-1}). The $MnS_{0.5}Se_{0.5}$@N-CNF //NVP@C full cell, assembled with $MnS_{0.5}Se_{0.5}$@N-CNF as anode and $Na_3V_2(PO_4)_3$@C as cathode, exhibits a high energy density of 254 Wh kg^{-1} can be provided. This work presents a novel strategy to optimize the design of anode materials through structural engineering and Se substitution, while also elucidating the underlying reaction mechanisms.

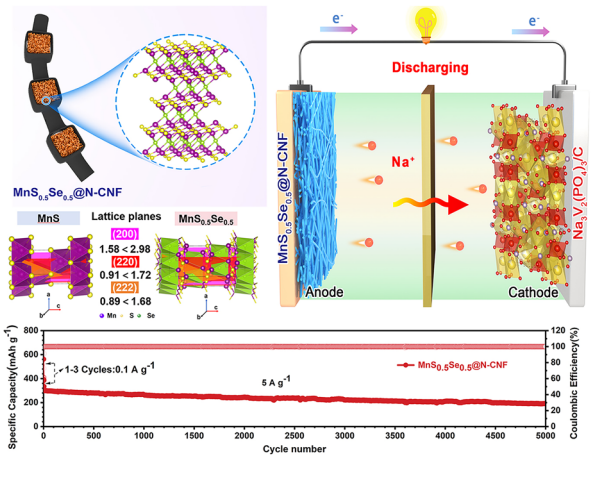

KEYWORDS Sodium-ion batteries; Anode; $MnS_{0.5}Se_{0.5}$; Carbon nanofiber; Defects

✉ Xiang Hu, huxiang@fjirsm.ac.cn; Junhua Xu, junhua.xu@gtk.fi; Zhenhai Wen, wen@fjirsm.ac.cn
[1] State Key Laboratory of Structural Chemistry, and Fujian Provincial Key Laboratory of Materials and Techniques Toward Hydrogen Energy, Fujian Institute of Research on the Structure of Matter, Chinese Academy of Sciences, Fuzhou 350002, People's Republic of China
[2] College of Chemistry, Fuzhou University, Fuzhou 350002, People's Republic of China
[3] State Key Laboratory of Clean Energy Utilization, Zhejiang University, Hangzhou 310027, People's Republic of China
[4] Geological Survey of Finland, P.O. Box 96, 02151 Espoo, Finland
[5] Key Laboratory of Advanced Energy Materials Chemistry (Ministry of Education), Nankai University, Tianjin 300071, People's Republic of China

Published online: 28 April 2025

Shanghai Jiao Tong University Press

Springer

1 Introduction

With the ever-increasing demand for electrically powered transportation vehicles, portable electronic devices, and renewable energy storage systems in modern society, the limited availability of lithium resources has posed significant challenges to the sustainable development of lithium-ion batteries (LIBs) for large-scale applications [1]. In contrast, sodium-ion batteries (SIBs) have emerged as a promising alternative to LIBs, due to the abundance of sodium (2.27% vs. lithium 0.002% of the Earth's crust), low cost, and relatively high environmental friendliness [2]. However, the larger ionic radius of Na^+ (0.102 nm vs. Li^+ 0.076 nm) and its greater atomic mass (22.99 g mol^{-1} vs. Li^+ 6.94 g mol^{-1}) make it more difficult for sodium-ions to intercalate and de-intercalate in anode materials, which results in SIBs still facing challenges in energy density, power performance, and cycle life [3–5]. Therefore, continuous technological innovation and material optimization are expected to further enhance the sodium storage performance of SIB anode materials.

Transition metal chalcogenides (TMSs) are considered promising anode materials for SIBs due to their high theoretical capacity and good electrochemical activity [6]. Among them, manganese sulfide (MnS) has attracted significant attention due to its advantages, such as abundant reserves, low cost, and a high theoretical capacity of up to 616 mAh g^{-1} [7]. However, the critical problems of the large volume changes, inherently mediocre conductivity, slow Na^+ reaction kinetics and high solubility of polysulfides during the continuous sodiation/desodiation process result in poor cyclability and inferior rate capability, which significantly hinders their practical applications [8–11]. In this regard, several strategies have been proposed to address these challenges: (i) the introduction of highly conductive carbon frameworks, which have proven effective in enhancing conductivity and providing structural support [12]. However, the poor interfacial binding between polar TMSs and non-polar carbon frameworks often leads to detachment of the active material from the carbon matrix during conversion reactions, severely affecting long-term cycle life [13]. (ii) Shrinking TMS particles to the nanoscale can effectively shorten the Na^+ diffusion path and expose more active sites to improve reaction kinetics [14]. Unfortunately, the high specific surface energy of nanoscale materials often leads to severe aggregation [15]. (iii) Constructing a heterogeneous structure by combining different TMSs can form abundant phase boundaries and increase electrochemically active sites [16, 17]. Despite numerous efforts to improve electrochemical performance, the reaction kinetics during long-term cycling may still be hindered by the uneven distribution of heterogeneous interface and the gradual passivation of interfacial reactions [18].

It has been reported that introducing exogenous anions to form single-phase ternary metal dichalcogenide compounds (MX_aX_{1-a}, X = S, Se, Te…) is an effective strategy for modulating the electronic structure of TMSs [19]. The uniqueness of this approach lies in the ability to precisely regulate the electronic structure of MX_aX_{1-a} at the atomic level [20, 21]. In particular, substituting Se as an anion in TMSs can significantly enhance their physicochemical properties. Firstly, Se, being in the same group as S, shares similar chemical properties, however, its atomic radius is smaller than that of S (1.98 vs. 1.84), and it has a smaller bandgap, which effectively enhances the electronic conductivity of TMSs and expands the lattice spacing [22]. Additionally, Se substitution creates new anion defect vacancies, promoting Na^+ storage capacity [23]. The M-Se bond is weaker than the M-S bond, making it more likely to break during the conversion reaction, thus facilitating faster Na^+ reaction kinetics [24]. Up to now, some MX_aX_{1-a} anode materials have been reported, such as MoSSe@Rgo [25], $CoS_{2-x}Se_x$@SG [26], $SnSe_{0.5}S_{0.5}$@NG [27]. However, there are few reports on single-phase anion-doped manganese-based anodes with precisely controlled Se substitution content for SIBs [28, 29]. The relationship and mechanism between selenium doping/substitution content and electrochemical performance have not yet been sufficient clarified. Therefore, it is essential to further investigate the balance of electrochemical reactions in these materials.

Herein, we first synthesized manganese carbonate ($MnCO_3$) nanocubes via the microemulsion precipitation method and mixed them with polyacrylonitrile. Subsequently, $MnCO_3$ nanofibers were formed using the electrospinning technique. During the subsequent carbonization process, the decomposition of $MnCO_3$ facilitated simultaneous sulfidation and selenization, enabling the controllable synthesis of $MnS_{0.5}Se_{0.5}$ porous nanocubes encapsulated in N-doped carbon nanofiber composite ($MnS_{0.5}Se_{0.5}$@N-CNF). The $MnS_{0.5}Se_{0.5}$ is firmly anchored in the carbon fibers through C–S–Mn and C–Se–Mn bonds, effectively alleviating volume expansion during cycling. The porous nanoscale $MnS_{0.5}Se_{0.5}$ cube not only prevent agglomeration of the active components, ensuring a short Na^+ diffusion path, but also accelerate the transfer of ions and electrons. Experimental

https://doi.org/10.1007/s40820-025-01767-4

results and theoretical calculations demonstrate that Se substitution enhances the electronic conductivity of MnS and promotes Na^+ diffusion kinetics. With these unique structural and compositional advantages, the $MnS_{0.5}Se_{0.5}$@N-CNF electrode exhibits excellent rate performance, high reversible capacity, and long-term cycling stability as the anode material for both sodium-ion half-cells and full cells.

2 Experimental Section

2.1 Chemicals

Manganese (II) Sulfate Monohydrate ($MnSO_4·H_2O$) were purchased from General Reagent. Sulfur sublimed (S), Cyclohexane (C_6H_{12}), 1-Butanol ($C_4H_{10}O$) and N,N-Dimethliformamide (C_3H_7NO) were purchased from Sinopharm Chemical Reagent Co., Ltd., China. Ammonium bicarbonate (NH_4HCO_3) were purchased from Macklin Reagent. Cetyltrimethylammonium ($C_{19}H_{42}BrN$) and Polyacrylonitrile ($(C_3H_3N)_n$) were purchased from Adamas beta. Selenium (Se) were purchased from Aladdin. All reagents and chemicals were of analytical grade and used without further purification.

2.2 Synthesis

2.2.1 Synthesis of $MnCO_3$ Nanocubes

In a typical synthesis process [30], 4 g of CTAB was dissolved in 100 mL of cyclohexane and 5 mL of n-butanol. After stirring evenly, 5 mL of 0.8 M NH_4HCO_3 aqueous solution was added. The mixed solution was stirred for 10 min until it became transparent. Then, 5 mL of 0.4 M $MnSO_4·H_2O$ aqueous solution was continuously added drop by drop to obtain a milky white solution. Subsequently, the precipitate was obtained by centrifugation, washed several times with water and ethanol, and then dried in an oven at 60 °C to obtain white $MnCO_3$.

2.2.2 Synthesis of $MnCO_3$@PAN Nanofibers by Electrospinning

$MnCO_3$@PAN was synthesized using a one-step electrospinning technique. Firstly, 1 g of $MnCO_3$ powder was added into 5 mL of DMF. After ultrasonic treatment for 2 h, a homogeneous dispersion was obtained. Then, 800 mg of polyacrylonitrile (PAN) was added into the mixture. After stirring at 75 °C for 12 h, a uniform solution was obtained. The uniformly mixed solution was transferred into a 10 mL syringe connected with a stainless steel needle (model 15) for electrospinning and then installed in the electrospinning device. During the entire electrospinning process, a positive voltage of 16 kV and a negative voltage of 2 kV were applied to the needle tube, and it was operated at a propulsion speed of 0.015 mL min^{-1}. The solution was ejected in the form of thin threads and collected on aluminum foil. The collected electrospun product was stabilized in air at 250 °C for 2 h.

2.2.3 Synthesis of $MnS_{0.5}Se_{0.5}$@N-CNF, MnS@N-CNF and MnSe@N-CNF Nanofibers

$MnS_{0.5}Se_{0.5}$@N-CNF was prepared by the simultaneous selenization and sulfidation method. Specifically, the precursor $MnCO_3$@N-CNF and the mixture of selenium and sulfur powders (with a mass ratio of M precursor: M (ms_e:ms = 1.51:1) = 1:2) were placed at the downstream and upstream of the quartz tube, respectively. Then, in a hydrogen-argon mixed atmosphere at 500 °C, the selenization/sulfidation was carried out for 2 h with a heating rate of 5 °C min^{-1}. In addition, the processes of adding only sulfur source or selenium source separately were the same as those for prepar $MnS_{0.5}Se_{0.5}$@N-CNF. Finally, the obtained samples were named MnS@N-CNF and MnSe@N-CNF, respectively.

2.3 Characterization

Analyzing the microstructure and morphology of samples by field emission scanning electron microscopy (FESEM, Hitachi SU-8020), field emission transmission electron microscopy (TEM, Tecnai G2 F20 S-TWIN TMP) and high-resolution transmission electron microscopy (HRTEM). Energy dispersive X-ray (EDX) spectroscopy was used to determine the distribution of elements. The crystalline phase structure of the sample was tested by X-ray powder diffractometer (XRD, Miniflex600 powder X-ray diffractometer with Cu Kαradiation). The Raman spectra were obtained by confocal Raman spectroscopy with a 532 nm light source

(LabRAM HR). Nitrogen adsorption/desorption isotherms from the Automatic Specific Surface and Porosity Analyzer (Micromeritics ASAP 2460). The defective condition of the sample was shown by the paramagnetic resonance spectrometer (EPR, Bruker-E500). The form of the chemical state in which the element exists is illustrated by the X-ray photoelectron spectrometer (XPS, Thermo Scientific K-Alpha). The carbon content of the samples was obtained by a comprehensive thermal analyzer (TGA, NETZSCH STA449F3) in a flow of air with a heating rate of 10 °C min^{-1}. To characterize the ex-situ XPS and TEM tests during the first cycle, the cells at different cut-off voltages were carefully disassembled inside an argon-filled glove box and the electrodes were washed in diethylene glycol dimethyl ether solvent for several times to remove residual electrolyte.

2.4 Electrochemical Measurements

The electrochemical testing was performed by assembly standard 2032 typed coin cells in an argon-filled glove box (< 0.01 ppm of moisture and oxygen contents). For the half-cell, the prepared active materials were used as the cathode, a homemade sodium metal sheet was used as anode, the electrolyte was 1.0 M $NaPF_6$ dissolved in diethylene glycol dimethyl ether (DIGLYME) and a glass fiber filter paper (GF/D, Whatman) was used as the separator. Preparation of the working electrode consists of a homogeneous slurry of containing active material (80 wt%), conductive carbon black (10 wt%) and sodium carboxymethyl cellulose (10 wt%) mixed in deionized water scraped and coated on the copper foil collector, subsequent drying in a 70 °C oven overnight. The active material loading mass approximately 0.8–1.0 mg cm^{-2}. Galvanostatic charging/discharging tests on a multi-channel LAND battery test system (Wuhan, China) with a potential range of 0.01–3.00 V at room temperature. Cyclic voltammetry (CV) curves were obtained using a CHI660E electrochemical workstation, and electrochemical impedance spectroscopy (EIS) was performed over a frequency range from 0.01 Hz to 100 kHz. The galvanostatic intermittent titration technique (GITT) tests were conducted under constant-current conditions at 0.05 A g^{-1} for 20 min, followed by rest intervals of 30 min after the third cycles.

For the construction of the $MnS_{0.5}Se_{0.5}$@N-CNF// $Na_3V_2(PO_4)_3$@C sodium-ion full cell, the cathode was fabricated through a specific process. A slurry was prepared by mixing $Na_3V_2(PO_4)_3$@C (NVP@C), conductive carbon black, and poly (vinylidene fluoride) (PVDF) in a weight ratio of 8:1:1 in N-methylpyrrolidone (NMP) solvent. This slurry was then cast onto aluminum current collectors and dried under vacuum at 80 °C overnight. The $MnS_{0.5}Se_{0.5}$@N-CNF electrode, after undergoing electrochemical activation to eliminate initial and irreversible capacity, functions as the anode. In all electrochemical tests, the electrolyte was 1.0 M $NaPF_6$ dissolved in DIGLYME for the full cell and NVP@C half-cell. It is remarkable that the cycling specific capacity of NVP@C at 0.1 A g^{-1} averages around 90 mAh g^{-1}. Therefore, to ensure a balanced capacity between the cathode and anode, the cathode/anode active mass ratio in the $MnS_{0.5}Se_{0.5}$@N-CNF// NVP@C full cell is precisely controlled to be approximately 5:1. The full cells were evaluated within a voltage range of 1.0 to 3.8 V in a multi-channel LAND battery test system at room temperature. The separator and the electrolyte utilized in the full cells were exactly the same as those employed in the half-cells.

3 Results and Discussion

3.1 Synthesis and Characterization of Samples

The synthesis process of $MnS_{0.5}Se_{0.5}$@N-CNF composites is schematically illustrated in Fig. 1a. Initially, highly uniform $MnCO_3$ nanocubes were prepared by the microemulsion precipitation method, exhibiting regular cubic shapes with side lengths of approximately 200 nm (Fig. S1a-c). Next, after being added to a DMF solution containing PAN, the $MnCO_3$ nanocubes were aligned in series by the electrospinning method, forming a unique nanofiber structure resembling a “necklace”. Finally, during the carbonization process, the solid $MnCO_3$ nanocubes underwent thermal decomposition while simultaneously undergoing selenization and sulfidation. This process led to the formation of hollow porous $MnS_{0.5}Se_{0.5}$ nanocages, which were embedded in and strung together by carbon nanofibers to obtain the “necklace”-shaped $MnS_{0.5}Se_{0.5}$@N-CNF composite.

The field emission scanning electron microscopy (FESEM) and TEM images of the $MnS_{0.5}Se_{0.5}$@N-CNF reveal a three-dimensional network structure where carbon nanofibers are interlaced and crossed in a staggered

 https://doi.org/10.1007/s40820-025-01767-4

manner, with nanocubes uniformly arranged within the carbon nanofibers (Fig. 1b–d). The magnified TEM image further shows that the $MnS_{0.5}Se_{0.5}$@N-CNF exhibits hollow porous nanocages encapsulated in carbon nanofibers, which effectively prevents the direct exposure of the $MnS_{0.5}Se_{0.5}$ nanocages to the electrolyte and enhance the conductivity of the composite (Fig. 1e) [31]. The selected-area electron diffraction (SAED) pattern displays multiple diffraction rings (Fig. S2), indicating the polycrystalline characteristics of $MnS_{0.5}Se_{0.5}$@N-CNF nanostructures. These diffraction rings can be indexed to the (200), (220), (222), and (400) crystal planes of $MnS_{0.5}Se_{0.5}$ [32]. The high-resolution TEM (HRTEM) image shows a parallel stacking structure with a large interlayer spacing of 0.265 nm corresponding to the (200) plane, and clearly reveals a carbon layer wrapping the surfaces of the $MnS_{0.5}Se_{0.5}$ nanocages (Fig. 1f). Additionally, lattice fringes with a spacing of 0.187 nm are observed, aligning well with the (220) plane of $MnS_{0.5}Se_{0.5}$. More importantly, as shown in Fig. 1g, the different colors in the lattice stripe images and the related fast Fourier transform (FFT)-filtered images are used to visualize the crystal defects in $MnS_{0.5}Se_{0.5}$@N-CNF, which are attributed to the increased disorder and distortion in the crystal structure caused by anion substitution of S with larger Se atoms. In comparison, the MnS@N-CNF exhibits a smaller interplanar spacing (0.213 nm) and fewer defects than $MnS_{0.5}Se_{0.5}$@N-CNF (Fig. 1h, i). The high-angle annular dark-field scanning TEM (HAADF-STEM) image of $MnS_{0.5}Se_{0.5}$@N-CNF and the corresponding energy-dispersive X-ray spectroscopy (EDX) elemental mappings reveal a homogeneous dispersion of $MnS_{0.5}Se_{0.5}$ nanocages within the carbon nanofibers (Fig. 1j). The EDX energy spectrum shows that the calculated atomic ratio of Mn:S:Se in $MnS_{0.5}Se_{0.5}$@N-CNF is approximately 1:0.5:0.5 (Fig. S3a, b). This ratio aligns with the elemental analysis results and corresponds to the stoichiometric ratio of $MnS_{0.5}Se_{0.5}$@N-CNF, confirming the successful introduction of Se species into the $MnS_{0.5}Se_{0.5}$@N-CNF lattice. Moreover, the morphologies of the MnS@N-CNF and MnSe@N-CNF composites, as revealed by SEM and TEM observations, show a similar network structure with carbon nanofibers interlaced and crossed in a staggered manner, while nanocubes uniformly arranged within the carbon nanofibers (Figs. S4 and S5).

The phase composition and crystal structure of the materials were identified through X-ray powder diffractometer (XRD) measurements. As shown in Fig. 2a, the main diffraction peaks from the sample $MnS_{0.5}Se_{0.5}$@N-CNF can belongs to the cubic crystal system with a Fm-3 m (225) space group (JCPDS No.01-089-4955) [33]. Notably, the (200), (220), and (222) planes of $MnS_{0.5}Se_{0.5}$@N-CNF present a significant shift to lower angles, indicating an expansion of the lattice spacing due to the incorporation of larger Se atoms into MnS at the atomic level, which is consistent with the TEM observations. To evaluate the impact of Se atoms on the crystal structure, we analyzed the structural characteristics using Rietveld-refined XRD. As can be seen from Figs. 2c and S6b, c, the XRD patterns of all samples are consistent with a cubic crystal system structure, resembling that of NaCl-type structure. In this structure, manganese ions occupy the positions of sodium-ions, while sulfur or selenium ions randomly replace the chloride ions. Figure 2b displays the three crystal planes (200), (220), and (222) of $MnS_{0.5}Se_{0.5}$ are larger than those of MnS, indicating that the incorporation of Se induces additional distortions in the crystal lattice, resulting in an expanded layer spacing that facilitates rapid Na^+ diffusion. Moreover, the Mn-Se bond differs from the Mn-S bond due to the different electronegativity and bonding characteristics of Se, which alter the electronic structure of the material and cause charge redistribution within the MnS lattice [34]. This may lead to the formation of defects such as vacancies, interstitials, and antisite defects (where atoms occupy incorrect lattice positions), as confirmed by the electron paramagnetic resonance (EPR) spectrum (Fig. 2d) [35]. The symmetric Lorentzian line at a g-value of 2.003 for $MnS_{0.5}Se_{0.5}$@N-CNF, shows a stronger signal compared to MnS@N-CNF and MnSe@N-CNF, indicating a higher concentration of defects and more active sites.

Raman spectroscopy was also examined to verify the chemical composition and structure. As shown in Fig. 2e, the Raman spectra of $MnS_{0.5}Se_{0.5}$@N-CNF clearly reveal three characteristic peaks. The first peak, located in the Raman shift region of 580–700 cm^{-1}, corresponds to the intrinsic vibrational modes of Mn-S and Mn-Se [36]. The intensity of this peak is higher than that of MnS@N-CNF and MnSe@N-CNF, indicating the successful complexation of S and Se with Mn, which is consistent with the XRD results. Two additional significant peaks, centered at ~ 1353 and ~ 1582 cm^{-1}, correspond to typical features of sp^3 hybridized disordered carbon (D-band) and sp^2 hybridized graphitic carbon (G-band) [37]. The I_D/I_G ratios of

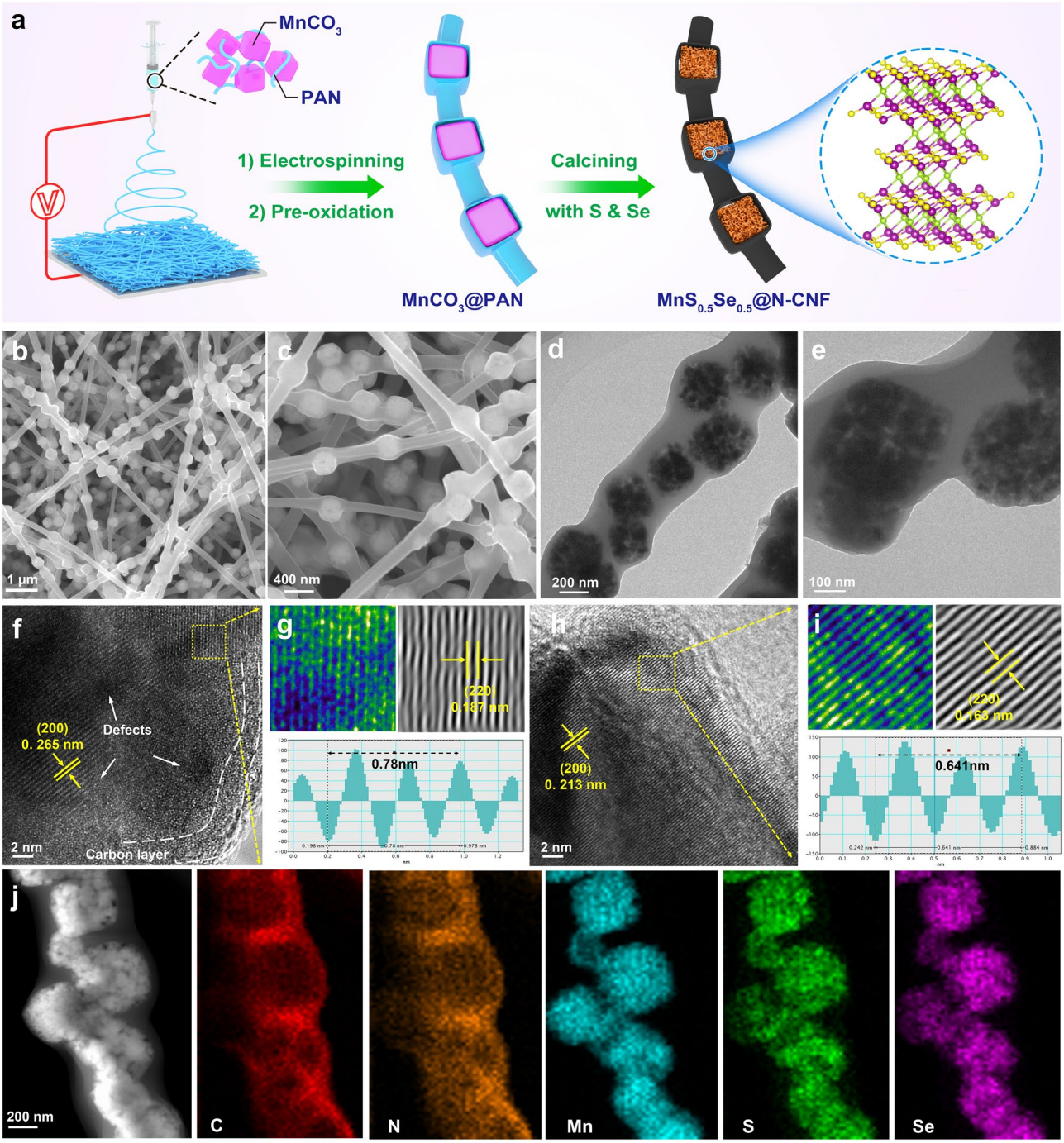

Fig. 1 **a** Schematic strategy of synthesis for the $MnS_{0.5}Se_{0.5}$@N-CNF composites, **b**, **c** FESEM images and **d**, **e** TEM images of $MnS_{0.5}Se_{0.5}$@N-CNF, **f**, **g** and **h, i** HRTEM image and related lattice stripe marking images with FFT-filtered of $MnS_{0.5}Se_{0.5}$@N-CNF and MnS@N-CNF, **j** EDS elemental mappings of $MnS_{0.5}Se_{0.5}$@N-CNF composite

$MnS_{0.5}Se_{0.5}$@N-CNF, MnS@N-CNF and MnSe@N-CNF were calculated to be ≈1.28, 1.21, and 1.24, respectively. The higher I_D/I_G ratio of $MnS_{0.5}Se_{0.5}$@N-CNF indicates that introducing Se atoms disrupts the symmetry of the carbon layer, resulting in a higher content of disordered carbon and an increased defect concentration within the carbon layer of the composite [38]. The weight percentage of carbon nanofiber (N-CNF) in the $MnS_{0.5}Se_{0.5}$@N-CNF composites

https://doi.org/10.1007/s40820-025-01767-4

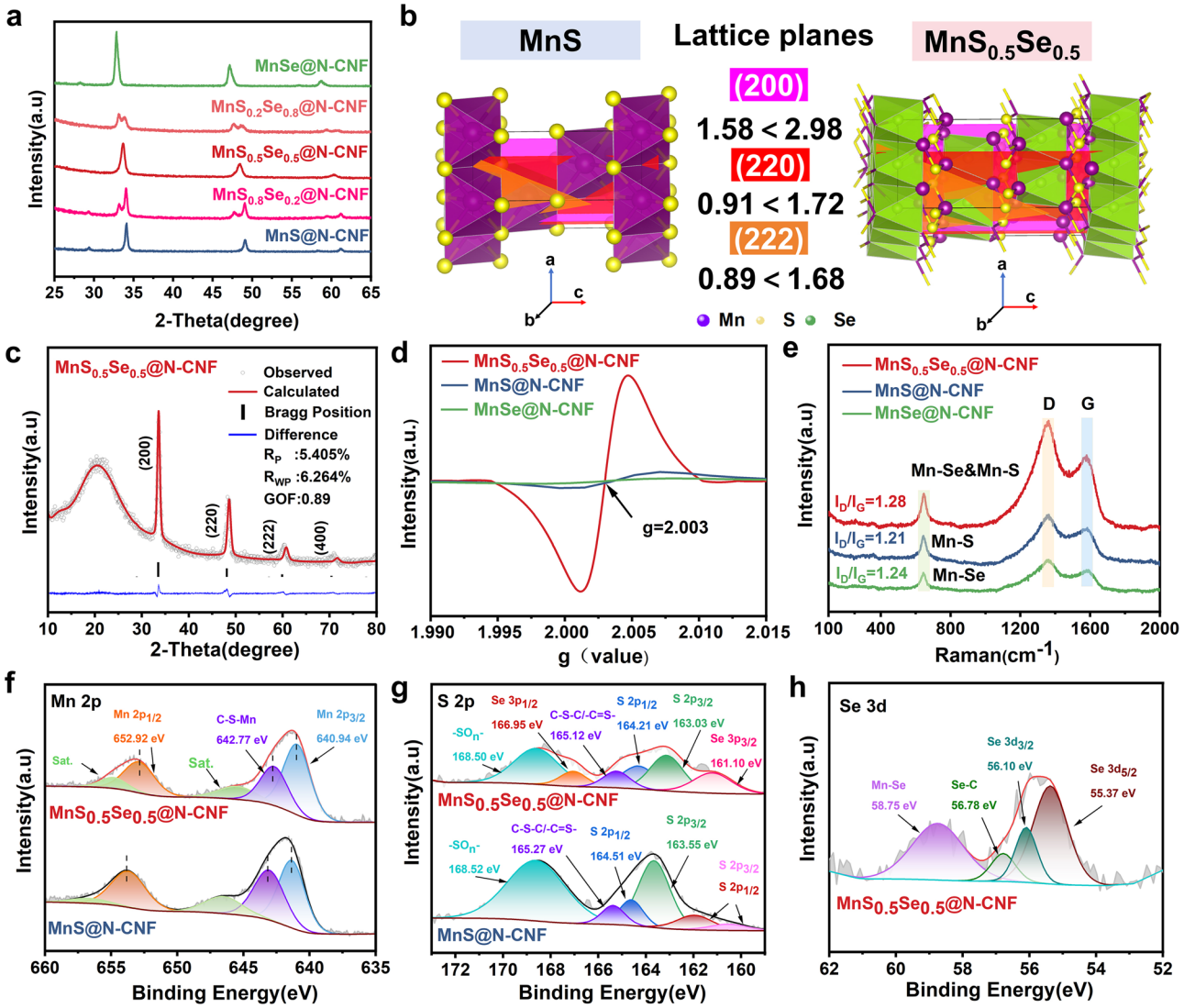

Fig. 2 XRD patterns of **a** as-prepared Mn-based chalcogenide MnS_xSe_{1-x}@N-CNF. **b** Crystal structures of $MnS_{0.5}Se_{0.5}$ and MnS. **c** Rietveld-refined XRD result of the $MnS_{0.5}Se_{0.5}$@N-CNF sample. **d**, **e** Electron paramagnetic resonance results and Raman spectra for $MnS_{0.5}Se_{0.5}$@N-CNF, MnS@N-CNF and MnSe@N-CNF. **f** High-resolution XPS spectra of Mn 2*p*, and **g** high-resolution XPS spectra of S 2*p* for $MnS_{0.5}Se_{0.5}$@N-CNF and MnS@N-CNF. **h** High-resolution XPS spectrum of Se 3*d* in the $MnS_{0.5}Se_{0.5}$@N-CNF

was analyzed using thermogravimetric analysis (TGA) under air condition (Fig. S7). The exothermic peak in the differential thermogravimetry curve (red line in Fig. S7a) aligns with the weight loss curve, indicating chemical reactions and phase transitions. Based on the final residual weight, which was verified by the XRD pattern (Fig. S7b, c), the mass content of $MnS_{0.5}Se_{0.5}$ in $MnS_{0.5}Se_{0.5}$@N-CNF composite is calculated as about 88.9%, and the corresponding weight percentage of N-CNF in the sample is estimated to be 11.1%. The carbon nanofiber (N-CNF) content in MnS@N-CNF and MnSe@N-CNF composite materials are estimated to be approximately 31.5% and 42.3%, respectively. The specific area and pore structure of the samples were investigated by nitrogen adsorption/desorption measurements, as shown in Fig. S8a. All samples exhibit type-IV isotherms with a distinctive hysteresis loop in the relative pressure range of 0.46–0.94, suggesting the presence of micro-/mesoporous structures [39]. Furthermore, the $MnS_{0.5}Se_{0.5}$@N-CNF exhibits a greater specific Brunauer–Emmett–Teller (BET) surface area of 23.37 $m^2\ g^{-1}$ in comparison with that of the MnS@N-CNF (12.28 $m^2\ g^{-1}$) and MnSe@N-CNF (19.74 $m^2\ g^{-1}$). The Barrett-Joyner-Halenda (BJH) pore size

distribution plot (Fig. S8b) reveals that $MnS_{0.5}Se_{0.5}$@N-CNF has a wider variety of pore types, including microporous, mesoporous, and macroporous structures. The high porosity not only provides numerous channels for Na^+ diffusion and storage within the electrode but also offers sufficient buffer space to accommodate the volume expansion of $MnS_{0.5}Se_{0.5}$@N-CNF during cycling.

X-ray photoelectron spectroscopy (XPS) was utilized to evaluate the surface electronic states and functional groups present in the synthesized samples. The XPS survey spectrum confirmed that the chemical composition of $MnS_{0.5}Se_{0.5}$@N-CNF includes elements such as Mn, S, Se, C, N, and O, as displayed in Fig. S9a, which is consistent with the results obtained from EDX mapping analysis. In the high-resolution C 1*s* spectra (Fig. S9d), distinct signals at binding energies of 284.5, 285.6, 286.6, and 288.1 eV correspond to C–C/C=C, C–N/C–O, C–N/C–S, and C=O groups, respectively [40]. The presence of N-doped species in the material is further confirmed by the high-resolution N 1*s* spectrum shown in Fig. S9g, which reveals four distinct nitrogen species: pyridinic N (398.4 eV), pyrrolic N (399.8 eV), graphitic N (400.8 eV), and oxygenated N (402.4 eV) [31]. Notably, the increase in graphitic N content with Se incorporation enhances both Na^+ and electron transport capabilities in the $MnS_{0.5}Se_{0.5}$@N-CNF. The nitrogen content in the $MnS_{0.5}Se_{0.5}$@N-CNF composite is 12.2 at%, compared to 9.5 at% in the MnS@N-CNF composite. The high-resolution Mn 2*p* spectrum (Fig. 2f) reveals three peaks at 652.9, 642.7, and 640.9 eV. The peaks at 652.9 and 640.9 eV correspond to Mn $2p_{1/2}$ and Mn $2p_{3/2}$, respectively, indicating the presence of Mn^{2+}. Additionally, the smaller peak at 642.7 eV likely represents the formation of C–S–Mn bonds between MnS and the carbon matrix [41]. Interestingly, the Mn 2*p* peaks of $MnS_{0.5}Se_{0.5}$@N-CNF shift to lower binding energies, indicating a reduction in the oxidation state of Mn due to bonding with the less electronegative Se atoms. This shift suggests that Se substitution tunes the d-band electronic structure of Mn atoms. In the S 2*p* high-resolution spectra (Fig. 2g), the spectra can be deconvoluted into four peaks. A pair of peaks at 163.03 and 164.21 eV corresponds to the S $2p_{3/2}$ and S $2p_{1/2}$ orbitals of Mn-S bond, while peaks at 161.10 and 166.95 eV are attributed to Se $3p_{3/2}$ and Se $3p_{1/2}$, respectively [6, 42]. Compared with that of MnS@N-CNF sample, both Mn 2*p* and S 2*p* for the $MnS_{0.5}Se_{0.5}$@N-CNF shift to lower binding energies, which is due to the incorporation of Se^{2-} into the MnS crystal lattice, resulting in a less electronegative chemical environment and lower binding energy of Mn-S. The peak at 165.12 eV is likely due to the formation of C–S bonds, possibly resulting from the interaction between sulfur and the carbon substrate, while the peak at 168.50 eV may be related to oxidized-S species formed upon exposure to air [43]. The high-resolution Se 3*d* spectra of the $MnS_{0.5}Se_{0.5}$@N-CNF in Fig. 2h present two typical peaks at the binding energies of 55.37 and 56.10 eV associating with the Se $3d_{5/2}$ and Se $3d_{3/2}$, respectively, characteristic of Se^{2-} (Mn–Se) [44]. Additionally, a peak at 56.78 eV indicates the presence of Se–C bonds, and the peak at 58.75 eV is attributed to SeO_x, resulting from the oxidation of Se^{2-} in the air [45]. These results provide insights into the chemical bonding and electron transfer in the C–Mn/C–S/C–Se architecture of $MnS_{0.5}Se_{0.5}$@N-CNF, which not only reduces the electron polarization but also accelerate the Na^+ and electron transfer.

3.2 Test and Analysis of Electrochemical Properties of the Samples

The electrochemical performance of the prepared composite anodes for sodium-ion storage was initially evaluated using half-coin cells with metallic sodium foil as the counter/reference electrode. The typical cyclic voltammetry (CV) curves of $MnS_{0.5}Se_{0.5}$@N-CNF for the initial three cycles, measured at a scan rate of 0.1 mV s^{-1} within the voltage window of 0.01–3.00 V, are shown in Fig. S10. During the first cathodic scan, two relatively weak peaks appeared at approximately 1.58 and 2.08 V, which can be attributed to the multi-step intercalation of Na^+ into the interlayers of $MnS_{0.5}Se_{0.5}$@N-CNF without phase transition [6]. Subsequently, two sharp reduction peaks at around 0.60 and 0.10 V are likely due to the conversion reaction, resulting in the formation of metallic Mn and Na-S/Na-Se compounds, accompanied by the formation of an irreversible solid electrolyte interface (SEI) film [46]. In the subsequent anodic scan, the oxidation peaks at approximately 1.54, 2.02, and 2.10 V correspond to the stepwise desodiation reactions [47]. In the subsequent anodic scan, the oxidation peaks at approximately 1.54, 2.02, and 2.10 V correspond to the stepwise desodiation reactions. The $MnS_{0.5}Se_{0.5}$@N-CNF electrodes show higher peak currents compared to MnS@N-CNF and MnSe@N-CNF, further demonstrating that the introduction of Se enhances the electrochemical reaction

https://doi.org/10.1007/s40820-025-01767-4

activity. In the subsequent cycles, the $MnS_{0.5}Se_{0.5}$@N-CNF electrodes displayed nearly overlapping redox peaks, indicating improved stability and reversibility of the Na^+ storage reaction process after Se doping.

Furthermore, in-situ XRD, ex-situ XPS, and ex-situ HRTEM were employed to characterize the structural transformation and phase evolution of $MnS_{0.5}Se_{0.5}$@N-CNF. Figure 3a shows the in-situ XRD patterns of $MnS_{0.5}Se_{0.5}$@N-CNF for the sodiation/desodiation processes. The peak at around 38.5°, 41.2°, 43.9°, and 45.8° belongs to the Be and BeO, which are attributed to the in-situ cell window [26]. The contour plot reveals prominent diffraction peaks at 33.5° in the pristine $MnS_{0.5}Se_{0.5}$@N-CNF, corresponding to the (200) plane. As the discharge process to 1.5 V, the characteristic peaks shifted to lower angles, indicating the insertion of Na^+ into $MnS_{0.5}Se_{0.5}$, forming an intermediate $Na_xMnS_{0.5}Se_{0.5}$. When the electrode is further discharged to 0.60 V, the distinct peaks from $Na_xMnS_{0.5}Se_{0.5}$ gradually increase in intensity. Meanwhile, new peaks appear at ≈22.6° and 37.3°, corresponding to the (111) and (220) planes of Na_2Se (JCPDS No. 04-003-6921), and at ≈23.5° and 38.9°, corresponding to the (111) and (220) planes of Na_2S (JCPDS No. 01-071-4842). When the electrode is fully discharged to 0.01 V, the Na_2Se and Na_2S signal still remains, and weak characteristic diffraction peaks appear at 48.0°, corresponding to metallic Mn (JCPDS No. 99-000-2278). The intensity of the $Na_xMnS_{0.5}Se_{0.5}$ peaks gradually weakens, indicating the conversion reaction between $Na_xMnS_{0.5}Se_{0.5}$ and Na^+, forming metallic Mn, Na_2Se, and Na_2S. During the charging process, the Na_2S and Na_2Se peaks gradually weaken and almost disappear by the end of the charge (3.00 V), suggesting that the conversion reaction between Na_2S, Na_2Se and Mn allows the original $MnS_{0.5}Se_{0.5}$ phase to fully recover, which is consistent with other reported manganese-based compound electrodes for SIBs [9, 16].

Subsequently, ex-situ XPS was employed to further analyze the changes in the valence state of $MnS_{0.5}Se_{0.5}$@N-CNF during cycling. As shown in Fig. 3b, the high-resolution Mn 2*p* spectrum reveals that when the electrode is discharged from 0.60 to 0.01 V, the Mn 2*p* peak shifts significantly toward lower binding energy. Notably, a clear characteristic peak of Mn^0 2*p* is observed, which may result from the reaction between Na^+ and $MnS_{0.5}Se_{0.5}$ [48]. Upon charging the electrode back to 3.00 V, the Mn^0 peak disappears completely, and the Mn 2*p* peak subtly shifts toward higher binding energy, closely matching the pristine state. A similar trend is observed in the high-resolution spectra of S 2*p* and Se 3*d* (Fig. S12a, b), where the energy shift toward lower binding energies from 0.60 V to the fully discharged state and the corresponding intensity changes are even more pronounced. These results indicate strong chemical bonding between Na^+ and heteroatom-doped active sites, suggesting the formation of Na_2S and Na_2Se [6]. Upon reverse charging to 3.00 V, the peak intensities of S and Se increase, and their binding energies shift back to higher values, confirming that the electrochemical reaction exhibits good reversibility.

The physical phase transformation of $MnS_{0.5}Se_{0.5}$@N-CNF was further verified by ex-situ HRTEM characterization. As depicted in Fig. 3c, d, after discharging the pristine $MnS_{0.5}Se_{0.5}$ phase to 0.60 V, the lattice fringes of the (200) crystal plane expand slightly to 0.278 nm due to Na^+ uptake. Additionally, interplanar spacings of 0.205 and 0.231 nm are observed, corresponding to the (311) crystal plane of Na_2Se and the (220) plane of Na_2S, respectively [27]. Upon further discharge to 0.01 V, the interplanar spacings of the final product are 0.231, 0.241, 0.209, 0.199, and 0.189 nm, corresponding to the (220) plane of Na_2S, the (220) plane of Na_2Se, and the (101), (111), and (110) planes of metallic Mn, respectively [6]. The corresponding SAED pattern displays a series of diffraction rings (Fig. 3g, h), corresponding to the cubic Mn (JCPDS No. 99-000-2278), cubic Na_2S (JCPDS No. 01-071-4842), and Na_2Se (JCPDS No. 04-003-6921), confirming the conversion processes. The EDS element mapping from STEM images shown in Fig. 3k further confirms that the carbon nanofiber-encapsulated porous nanocube structure is well maintained, with Mn, S, Se, and Na uniformly distributed within the C matrix, demonstrating high structural stability. Upon charging to 1.50 V, the SAED pattern (Fig. 3i) and HRTEM result (Fig. 3e) show the Na_2S/Na_2Se underwent partial transformation into $MnS_{0.5}Se_{0.5}$, with some Na_2S and Na_2Se remaining. Simultaneously, the lattice fringe of Mn disappears, demonstrating the Na-ion extraction process. Upon charging to 3.00 V, the diffraction rings and lattice fringes of Na_2S and Na_2Se disappear, replaced by those of the $MnS_{0.5}Se_{0.5}$, indicating the highly reversible conversion reaction (Fig. 3f, j). From the above results, the $MnS_{0.5}Se_{0.5}$@N-CNF exhibits a stepwise electrochemical process, with synergistic effects between the conversion and Na-ion (de)intercalation reactions, as visually represented in Fig. 3l. Overall, the detailed

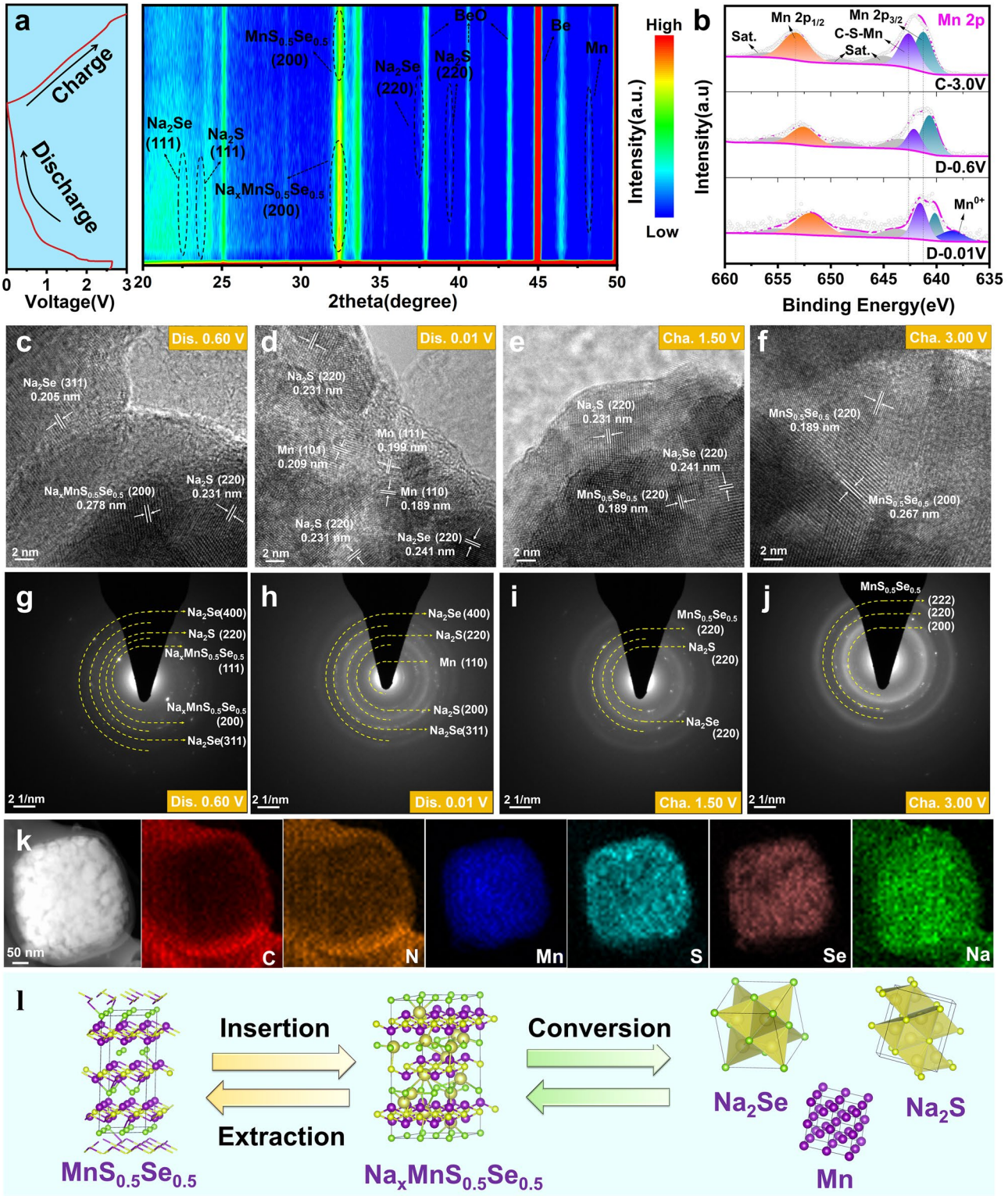

Fig. 3 **a** In situ XRD with a 2D contour plot of the $MnS_{0.5}Se_{0.5}$@N-CNF electrode during the initial cycle. **b** High-resolution XPS Mn 2*p* spectra of the $MnS_{0.5}Se_{0.5}$@N-CNF electrode at different initial discharged and charged states. Ex-situ HRTEM images and the corresponding selected-area electron diffraction patterns of the $MnS_{0.5}Se_{0.5}$@N-CNF electrode at different initial discharged and charged states: **c**, **g** discharged state of 0.60 V, **d**, **h** discharged state of 0.01 V, **e**, **i** charged state of 1.50 V, **d**, **h** charged state of 3.00 V, and **k** EDS elemental mappings of discharging to 0.01 V. **l** The corresponding schematic illustration of Na^+ storage mechanism for the $MnS_{0.5}Se_{0.5}$@N-CNF composite

https://doi.org/10.1007/s40820-025-01767-4

working processes of $MnS_{0.5}Se_{0.5}$@N-CNF is summarized as follows:

Sodiation Process:

(i) $MnS_{0.5}Se_{0.5} + xNa^+ + xe^- \rightarrow Na_xMnS_{0.5}Se_{0.5}$

(ii) $Na_xMnS_{0.5}Se_{0.5} + (2-x)\ Na^+ + (2-x)\ e^- \rightarrow Mn + 0.5Na_2S + 0.5Na_2Se$

Desodiation Process:

(iii) $Mn + 0.5Na_2S + 0.5Na_2Se \rightarrow MnS_{0.5}Se_{0.5} + 2Na^+ + 2\ e^-$

Due to its well-designed nanostructure, excellent sodium storage reversibility, and high defect concentration, the carbon nanofiber-encapsulated porous nanocube $MnS_{0.5}Se_{0.5}$@N-CNF nanocomposite is expected to exhibit outstanding performance in SIBs. Figure S13a-c shows the galvanostatic charge–discharge (GCD) curves of each sample for the initial three cycles at 0.1 A g^{-1}, where the corresponding voltage platforms align well with the redox behaviors observed in the CV results. The $MnS_{0.5}Se_{0.5}$@N-CNF electrode delivers an initial discharge and charge capacities of 613.2/556.8 mAh g^{-1}, corresponding to a high initial Coulombic efficiency (ICE) of 90.8%, which is higher than that of MnS@N-CNF (682.2/553.0 mAh g^{-1}, 81.1%). Such high ICE of $MnS_{0.5}Se_{0.5}$@N-CNF exceeds the values reported for other metal dichalcogenides with multiple anions (Fig. 4a) [49–57]. The improvement in the ICE of the $MnS_{0.5}Se_{0.5}$@N-CNF electrode in SIBs can be attributed to the following factors: 1) the substitution of S by Se causes lattice distortion, which expands the ion channels, facilitating Na^+ diffusion, 2) the incorporation of carbon nanofibers improves electrical conductivity while also providing mechanical support, maintaining the structural integrity, 3) the strong interfacial interaction between $MnS_{0.5}Se_{0.5}$ and the carbon nanofibers contributes to the formation of a stable SEI film. These aspects promote the reversible reaction of sodium-ions, reduce irreversible losses and capacity degradation in multiple ways. Moreover, the capacity of $MnS_{0.5}Se_{0.5}$@N-CNF electrode gradually increases after the initial cycles and begins to stabilize after 100 cycles, demonstrating a relatively high and stable reversible capacity of 595.1 mAh g^{-1} after 200 cycles (Fig. S14). This increase is likely due to the pulverization of $MnS_{0.5}Se_{0.5}$ nanoparticles, which creates more active sites for Na^+ storage. In contrast, the MnSe@N-CNF electrode exhibits a similar phenomenon, with its capacity sharply decaying after 100 cycles before stabilizing at 343.6 mAh g^{-1} after 200 cycles. The capacity of MnS@N-CNF, however, continuously decays from 537.0 to 181.0 mAh g^{-1} after 200 cycles. Moreover, the morphology of $MnS_{0.5}Se_{0.5}$@N-CNF still maintains its original structure after a long cycle of charge and discharge (Fig. S15), indicating that it has excellent structural stability. Charge–voltage curves collected at different cycles further confirm the stable and reversible Na^+ reactions of the $MnS_{0.5}Se_{0.5}$@N-CNF electrode (Fig. 4b). However, for the MnS@N-CNF electrode, the peaks around 1.5–2.2 V weaken and eventually disappear with increasing cycles, corresponding to the conversion reaction of MnS. This indicates that during electrode pulverization, the shuttle effect of polysulfide intermediates becomes severe, leading to poor structural integrity (Fig. 4c). Furthermore, the $MnS_{0.5}Se_{0.5}$@N-CNF electrode delivered superior rate performance (Fig. 4d). The capacities for $MnS_{0.5}Se_{0.5}$@N-CNF are 520.9, 514.5, 507.7, 486.5, 467.2, 446.8, 427.8, 418.3, and 405.2 mAh g^{-1} at 0.05, 0.1, 0.2, 0.5, 1, 2, 3, 4, and 5 A g^{-1}, respectively. Notably, it achieves a high reversible capacity of 370.5 mAh g^{-1} even at a high current density of 10 A g^{-1}. When the current density is restored to 0.1 A g^{-1}, a high average reversible capacity of 539.5 mAh g^{-1} can be maintained, and the capacity continues to grow, demonstrating rapid redox reactions and low polarization. In contrast, under the same testing conditions, MnS@N-CNF electrodes exhibit rapid capacity decay from 524.5 to 161.9 mAh g^{-1}. The rate performance of $MnS_{0.5}Se_{0.5}$@N-CNF is significantly better than that of MnS@N-CNF and MnSe@N-CNF, standing out among other reported MnSe and MnS-based anodes for SIBs (Fig. 4e) [7, 36, 40, 58–64]. In addition, the discharge/charge voltage curves are stable, with the electrode polarization increasing slowly (Fig. S16a-c), further confirming the strong stability and excellent Na^+ capturing ability of $MnS_{0.5}Se_{0.5}$@N-CNF as the current density increases, which is crucial for high-power battery applications. Moreover, the $MnS_{0.5}Se_{0.5}$@N-CNF electrode exhibited outstanding rate performance even under high mass loading, as shown in Fig. S17. The areal capacity increases nearly linearly with current density from 0.1 to 5 A g^{-1} when the mass loading is up to 2.9 mg cm^{-2}. However, at a higher mass loading of 4.1 mg cm^{-2}, the areal capacity deviates from linearity and begins to

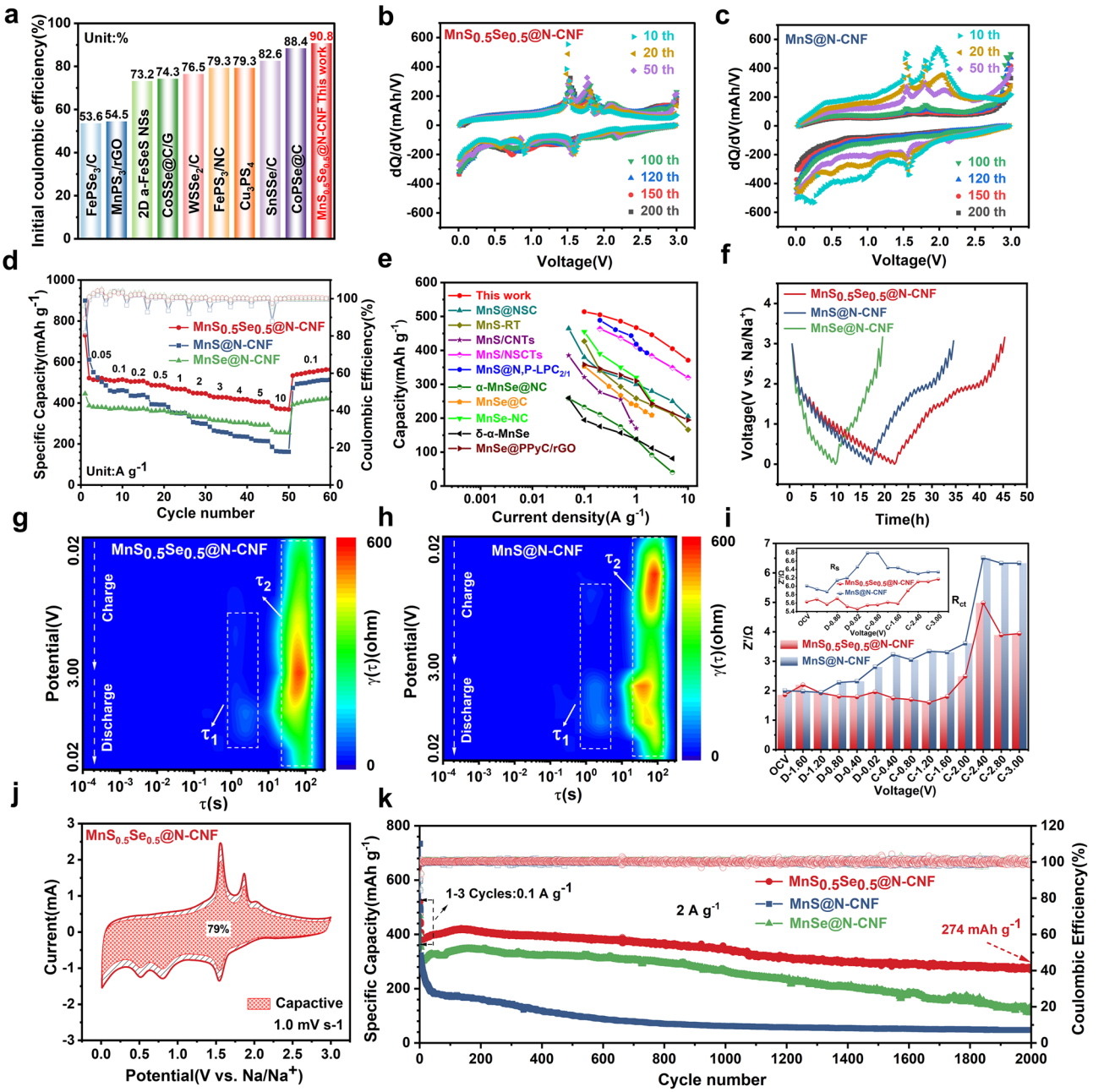

Fig. 4 **a** Comparison of ICE at 0.1 A g^{-1}, **b** differential charge versus voltage curve of $MnS_{0.5}Se_{0.5}$@N-CNF and **c** MnS@N-CNF electrodes. **d** Rate performance of $MnS_{0.5}Se_{0.5}$@N-CNF, MnS@N-CNF and MnSe@N-CNF electrodes. **e** Comparison of rate performance of $MnS_{0.5}Se_{0.5}$@N-CNF with the reported MnSe and MnS-based anodes for SIBs. **f** GITT curves of $MnS_{0.5}Se_{0.5}$@N-CNF, MnS@N-CNF and MnSe@N-CNF electrodes. DRT contour plots from EIS measurements of **g** $MnS_{0.5}Se_{0.5}$@N-CNF and **h** MnS@N-CNF at different potentials. **i** The evolution of R_{SEI} and R_{ct} during cycling in $MnS_{0.5}Se_{0.5}$@N-CNF and MnS@N-CNF electrodes. **j** Capacitive contribution at 1.0 mV s^{-1} of the $MnS_{0.5}Se_{0.5}$@N-CNF electrode. **k** Long-term cycling performance of the $MnS_{0.5}Se_{0.5}$@N-CNF, MnS@N-CNF and MnSe@N-CNF electrodes at 2.0 A g^{-1}

plateau. This phenomenon can be attributed to charge transport limitations within the electrolyte at such high mass loading, where the penetration depth of the ionic current becomes insufficient, leading to reduced utilization of active materials. Nevertheless, across different mass loadings, the capacity of the $MnS_{0.5}Se_{0.5}$@N-CNF electrode consistently returns to its initial state when the current

https://doi.org/10.1007/s40820-025-01767-4

density is restored to 0.1 A g^{-1}, demonstrating its excellent reversibility.

3.3 Kinetic Analysis of the Samples

The galvanostatic intermittent titration technique (GITT) was used to in-situ evaluate the interfacial reaction resistance of as-prepared electrodes during the sodiation and desodiation processes. The $MnS_{0.5}Se_{0.5}$@N-CNF electrode exhibits smaller overpotentials and higher Na^+ diffusion coefficients (D_{Na+}) during both the Na^+ insertion and extraction processes compared to the MnS@N-CNF and MnSe@N-CNF electrode (Fig. S18), indicating improved Na^+ diffusion kinetics. This is further corroborated by in-situ electrochemical impedance spectroscopy (EIS) analyses, which reveal the impact of Se doping on charge transport kinetics. As shown in Fig. S19a, d, the EIS profiles of the $MnS_{0.5}Se_{0.5}$@N-CNF and MnS@N-CNF electrodes are similar, featuring a semicircle in the high-frequency region, corresponding to charge transfer resistance (R_{ct}) and SEI film resistance (R_s), and an oblique line in the low-frequency region corresponding to Warburg impedance (Z_w), which represents the diffusion of Na^+ ions [65]. To clarify this disparity and separate the overlapping electrochemical phenomena existing in conventional Nyquist plots, the distribution of relaxation time (DRT) analysis was adopted for quantitative deconvolution (Fig. S19b, c and e, f), and the corresponding contour plots were presented in Fig. 4g, h. The τ_1 peak (about 10^0–7.5×10^0 s) corresponds to the migration of Na^+ across the surface of the porous network. Due to the carbon nanofiber structure, MnS@N-CNF and $MnS_{0.5}Se_{0.5}$@N-CNF exhibit minimal impedance contributions during this process. The τ_2 peak (about 10^1–2×10^2 s) is associated with the ion diffusion impedance in the low-frequency region of the EIS, reflecting the deep diffusion of Na^+ into the bulk electrode. Compared with MnS@N-CNF, $MnS_{0.5}Se_{0.5}$@N-CNF has a larger specific surface area, which shortens the ion transport channels. Moreover, the introduction of Se improves the internal electronic structure of the material and accelerates the ion mobility, thus alleviating this diffusion limitation. The EIS curves of electrodes were fitted using an equivalent circuit (Fig. S20) [66]. Compared with MnS@N-CNF, the $MnS_{0.5}Se_{0.5}$@N-CNF electrode shows ultralow and highly stable charge transfer resistances across different (de)sodiation states (Fig. 4i), indicating the ultra-fast and robust reaction kinetics during continuous structural evolution. A kinetic study based on cyclic voltammetry (CV) curves at various scan rates was conducted to further understand the mechanism behind the rapid Na^+ ion storage in the $MnS_{0.5}Se_{0.5}$@N-CNF electrode. As depicted in Fig. S22a-c, compared with the CV curves of MnS@N-CNF and MnSe@N-CNF electrode, the $MnS_{0.5}Se_{0.5}$@N-CNF maintains a consistent CV shape as the scan rate increases from 0.2 to 1.2 mV s^{-1}, demonstrating minimal electrochemical polarization and excellent electrochemical reversibility during the charging/discharging process. The redox peak b value of the $MnS_{0.5}Se_{0.5}$@N-CNF electrode ranges from 0.51 to 1.37, with both cathodic and anodic peak currents higher than those of the MnS@N-CNF electrode (Fig. S22d-f), indicating that the electrode is primarily surface capacitance-controlled in its Na^+ storage mechanism. As shown in Fig. 4j, the $MnS_{0.5}Se_{0.5}$@N-CNF electrode makes a significant contribution to capacitance of 79.0% at 1.0 mV s^{-1}, which is higher than 61.0% of the MnS@N-CNF electrode (Fig. S23a). Moreover, when the scan rate increases from 0.2 to 1.2 mV s^{-1}, the capacitive contribution of the $MnS_{0.5}Se_{0.5}$@N-CNF electrode increases from 67.2% to 84.5%, which is significantly higher than that of the MnS@N-CNF electrode (Fig. S23b). These results indicate that the implantation of anion Se defects into metal sulfides is more conducive to surface-induced pseudocapacitive charge storage. The outstanding electrochemical kinetics of $MnS_{0.5}Se_{0.5}$@N-CNF is a key factor behind its excellent cycling stability, with a capacity of 274.0 mAh g^{-1} after 2000 cycles at 2 A g^{-1}, retaining 68.5% of its capacity retention. The capacity of the $MnS_{0.5}Se_{0.5}$@N-CNF electrode gradually increases after the initial cycles, which can be attributed to the continuous activation of active materials and the decomposition of electrolytes during cycling. In contrast, the MnS@N-CNF anode displays a much poorer cycling stability, with only 26.3% capacity retention after 2000 cycles (Fig. 4k). Moreover, the $MnS_{0.5}Se_{0.5}$@N-CNF anode maintains stable discharge/charge voltage profiles with minimal electrode polarization over prolonged cycling. In comparison, the MnS@N-CNF anode suffers from limited electrical conductivity, necessitating higher operating voltages to sustain performance. This leads to increased polarization, lower capacity output, and accelerated capacity degradation. Furthermore, the $MnS_{0.5}Se_{0.5}$@N-CNF anode also demonstrates highly stable cycling performance at 5 A g^{-1}, retaining 190.8 mAh g^{-1} after over 5000 cycles with

a capacity retention of 65.5% and nearly 100% Coulombic efficiency (Fig. S24). The excellent sodium storage performance of $MnS_{0.5}Se_{0.5}$@N-CNF is primarily attributed to its porous structure and nanofiber carbon framework, which mitigate volume expansion and maintain high structural integrity during Na^+ insertion and extraction. Additionally, the interfacial effect resulting from the incorporation of S and Se into the transition metal dichalcogenide promotes the transfer of interfacial electrons. Consequently, the $MnS_{0.5}Se_{0.5}$@N-CNF electrode is expected to be a high-capacity and durable anode material for SIBs.

3.4 DFT Analysis of the Influence of Se Doping on Na^+ Storage

To gain a deeper understanding of the significantly enhanced electrochemical activity and stability of $MnS_{0.5}Se_{0.5}$@N-CNF, we performed density functional theory (DFT) calculations to explore its structural advantages. First-principles calculations were conducted to investigate the impact of S/Se doping on Mn-based materials for Na^+ storage. The adsorption energy (ΔEa) of Na^+ on the activity sites in all configurations were calculated. As shown in Fig. 5b, MnSe (− 2.59 eV) and MnS (− 2.61 eV) exhibited a poor adsorption capacity for Na^+ (Figs. S26 and S27). However, with the introduction of Se and a few S atoms into the Mn-based materials, the Na^+ adsorption on the site was significantly enhanced, affording a ΔEa of $MnS_{0.5}Se_{0.5}$ (− 2.93 eV) (Fig. S25). This improvement in Na^+ adsorption can be attributed to the bonding between Se and S atoms, as well as the larger radius of the Se atom, which creates protruding structures on the Mn-based materials, increasing the interlayer spacing and boosting the sodium-ion energy storage capacity. To obtain a deeper perspective of the doping effects, the total DOS (TDOS) were essentially taken a deep perspective (Fig. 5d). The $MnS_{0.5}Se_{0.5}$ exhibited a higher DOS peak near the Fermi level after Se doping, indicating that Se facilitated the electrical conductivity of the materials. Furthermore, the $MnS_{0.5}Se_{0.5}$ shows higher reactivity of the active sites than others according to the associated the local Fermi softness analysis. Additionally, the charge density difference was examined to understand the bonding properties of the adsorbed Na^+ in the corresponding model (Fig. 5a). In the 2D projection of the charge density contour, $MnS_{0.5}Se_{0.5}$, MnS and MnSe were compared (Fig. 5c). The red and blue regions indicate higher and lower reactivity, respectively. The $MnS_{0.5}Se_{0.5}$ exhibited significantly more red areas, favoring more effective energy storage compared to the other two samples. To further investigate the fast kinetics of $MnS_{0.5}Se_{0.5}$, MnS and MnSe, the diffusion barrier energies and the minimum energy paths for Na^+ were calculated (Fig. 5e, f). $MnS_{0.5}Se_{0.5}$ exhibited the lowest diffusion energy barrier (0.34 eV) compared to MnS (0.42 eV) and MnSe (0.65 eV). This suggests that the Se and N dopants contribute to improved diffusion kinetics and reduced diffusion resistance for Na^+. In conclusion, the DFT results indicate that the excellent performance of $MnS_{0.5}Se_{0.5}$ can be attributed to the large number of defects, additional active sites, and the expansion of layer spacing caused by Se/S doping. These factors enhance the Na^+ adsorption capacity, leading to rapid electrochemical reaction kinetics and improved capacity performance for the anode.

3.5 Electrochemical Performance Tests in Sodium-Ion Full Cell

Additionally, a sodium-ion full cell was assembled via employing the $MnS_{0.5}Se_{0.5}$@N-CNF as anode and $Na_3V_2(PO_4)_3$@C (NVP@C) as cathode to further evaluate the application potential of SIBs device, as illustrated in the schematic diagram in Fig. 6a. The electrochemical properties and morphological characterizations of NVP@C are detailed in Fig. S28. Figure 6b shows the charge/discharge curves of the NVP@C cathode and $MnS_{0.5}Se_{0.5}$@N-CNF anode. The full cell exhibits a voltage difference between the cathode and anode. The integral calculation results in an operating voltage of 1.90 V during discharge. The charge/discharge curves for the first three cycles demonstrate excellent overlap, achieving a coulombic efficiency close to 100% (Fig. S29). The cycling performance is further illustrated in Fig. 6c, revealing a remaining reversible capacity of 77 mAh g^{-1} after 200 cycles, with a capacity retention of 85.6%. The capacity of the full battery is obtained based on the total mass of the positive and negative electrode materials. Moreover, the full cell demonstrates superior rate performance, with discharge capacities of 90.3, 87.2, 84.5, 82.1, 77.3, 67.2, and 48.9 mAh g^{-1} at the current densities of 0.05, 0.1, 0.2, 0.5, 1, 2, and 5 A g^{-1}, respectively (Fig. 6d). When the current density is reduced back to 0.1 A g^{-1}, a reversible capacity of 81.4 mAh g^{-1} can be recovered. The charge/discharge curves at different

https://doi.org/10.1007/s40820-025-01767-4

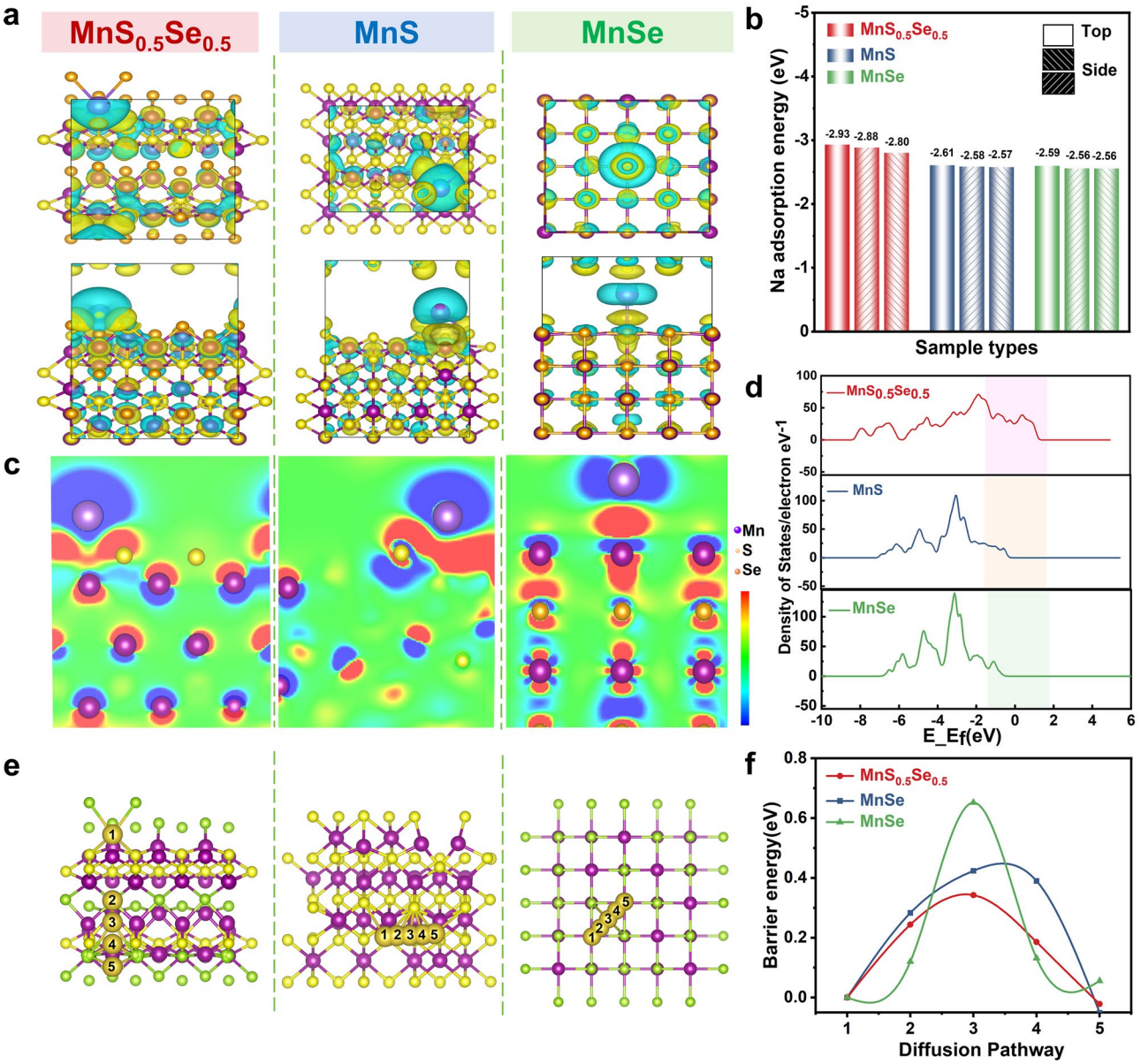

Fig. 5 **a** Na-ion adsorption energy at different active sites of $MnS_{0.5}Se_{0.5}$, MnS and MnSe. **b** Na-ion adsorption energy at different active sites of $MnS_{0.5}Se_{0.5}$, MnS and MnSe. **c** 2D projection of charge density contour of $MnS_{0.5}Se_{0.5}$, MnS and MnSe. **d** Density of states (DOS) of $MnS_{0.5}Se_{0.5}$, MnS and MnSe. **e** Illustration of the Na-ion diffusion path in $MnS_{0.5}Se_{0.5}$, MnS and MnSe. **f** Na^+ diffusion energy barriers of $MnS_{0.5}Se_{0.5}$, MnS and MnSe

current densities show minimal polarization, even at the high current density of 5 A g^{-1} (Fig. S30), verifying splendid rate ability. The calculated energy and power densities of $MnS_{0.5}Se_{0.5}$@N-CNF//NVP@C full cell are presented in Fig. 6e. The full cell delivers a maximum energy density of 254 Wh kg^{-1} at a power density of 141 Wkg^{-1}. Even at the high-power density of 13,650 W kg^{-1}, the energy density remains at 133.5 Wh kg^{-1}. This performance is comparable to, or even surpasses, that of some representative sodium-ion full cells reported in the literature [7, 19, 21, 67–72]. Moreover, the $MnS_{0.5}Se_{0.5}$@N-CNF//NVP@C full cell exhibits long cycle performance at 1.0 A g^{-1} (Fig. 6f), with a reversible capacity of 54 mAh g^{-1} after 500 cycles, demonstrating excellent durability. Additionally, a series of light-emitting diodes (LEDs) are successfully illuminated using two $MnS_{0.5}Se_{0.5}$@N-CNF//NVP@C button cells (inset

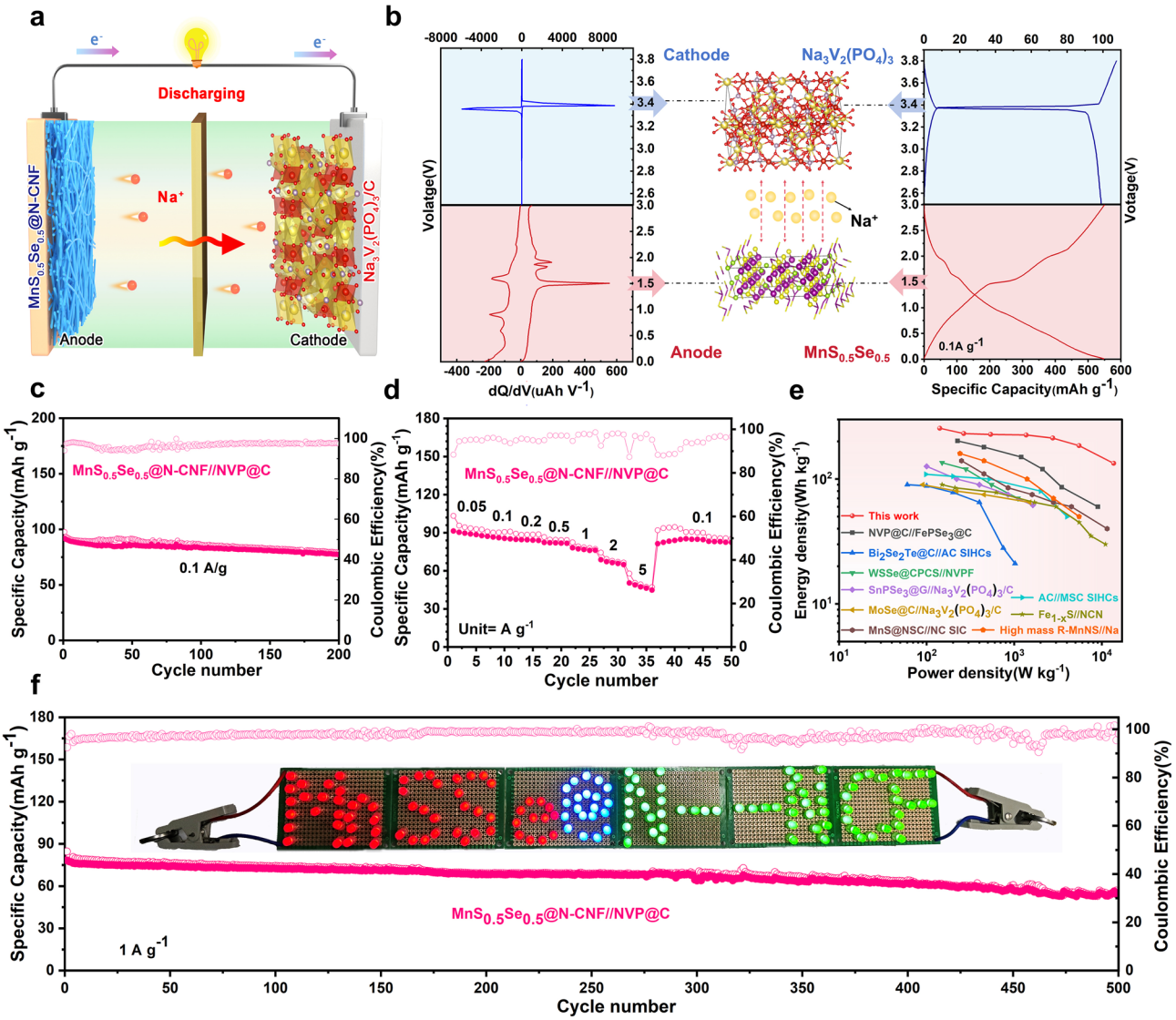

Fig. 6 **a** Schematic illustration of the sodium-ion full battery with $MnS_{0.5}Se_{0.5}$@N-CNF //NVP@C couple. **b** Electrochemical performances of the as-prepared full cell based on the $MnS_{0.5}Se_{0.5}$@N-CNF anode and NVP@C cathode: left) charge versus voltage curves and right) charge–discharge profiles of the corresponding half-cells. **c** Cycling stability at 0.1 A g^{-1}, and **d** rate performance of the full battery. **e** Comparison of the energy/power density of the $MnS_{0.5}Se_{0.5}$@N-CNF //NVP@C device with previously reported SIBs full battery. **f** Long-term cycle performance of the full cell at 1 A g^{-1} (Inset of photograph of different colors of LED lights powered by the full battery)

in Fig. 6f), further highlighting the potential for practical applications in the future.

4 Conclusions

In conclusion, we demonstrated the fabrication of necklace-like $MnS_{0.5}Se_{0.5}$@N-CNF using a simple electrospinning method. The porous and necklace-like nanofiber network structure provides an efficient ion transfer pathway and alleviates stress during the charge–discharge cycles. Comprehensive experimental investigations and DFT calculations indicate that the incorporation of Se not only helps to increase the active surface area and enhances the electrical conductivity, but also improves the adsorption capacity and decreases the migration energy barrier of Na^+, thus accelerating the electrochemical reaction kinetics and strengthening the cycling stability. Additionally, the structural

https://doi.org/10.1007/s40820-025-01767-4

evolution mechanism of $MnS_{0.5}Se_{0.5}$@N-CNF during the sodiation/desodiation process was studied using in-situ XRD, ex-situ TEM and XPS. Thanks to its unique hierarchical structure and the synergistic combination of components, the $MnS_{0.5}Se_{0.5}$@N-CNF electrode demonstrates a high specific capacity, outstanding rate performance (370.5 mAh g^{-1} at 10 A g^{-1}), and remarkable long-term cycling performance over 5000 cycles. Furthermore, when paired with $Na_3V_2(PO_4)_3$@C to form a $MnS_{0.5}Se_{0.5}$@N-CNF//NVP@C sodium-ion battery, the energy density reaches as high as 254 Wh kg^{-1}. This research effectively addresses the challenges associated with TMSs anode for SIBs and provides new insights for the development of advanced battery materials.

Acknowledgements This work was financially supported by the National Natural Science Foundation of China (No. 22225902, U22A20436, 22209185), National Key Research & Development Program of China (2022YFE0115900, 2023YFA1507101, 2021YFA1501500), the Self-deployment Project Research Program of Haixi Institutes, Chinese Academy of Sciences (No. CXZX-2022-GH04, CXZX-2023-JQ08), and Science and Technology Program of Fuzhou (2023-P-009).

Authors' Contributions Each author should specify their contributions to this paper. Such as, Puwu Liang: Investigation, Data curation, original draft writing. Duo Pan: Writing—theoretical calculation. Xiang Hu: Writing—review and editing. Ke R. Yang: Methodology. Yangjie Liu: Formal analysis. Zheng Bo: Investigation. Zijing Huo, Lihong Xu, Junhua Xu: Review. Zhenhai Wen: Supervision, Project administration, Funding acquisition.

Declarations

Conflict of Interest The authors declare no interest conflict. They have no known competing financial interests or personal relationships that could have appeared to influence the work reported in this paper.

Supplementary Information The online version contains supplementary material available at https://doi.org/10.1007/s40820-025-01767-4.

References

1. J. Xu, X. Cai, S. Cai, Y. Shao, C. Hu et al., High-energy lithium-ion batteries: recent progress and a promising future in applications. Energy Environ. Mater. **6**(5), e12450 (2023). https://doi.org/10.1002/eem2.12450
2. F. Hartmann, M. Etter, G. Cibin, L. Liers, H. Terraschke et al., Superior sodium storage properties in the anode material $NiCr_2S_4$ for sodium-ion batteries: an X-ray diffraction, pair distribution function, and X-ray absorption study reveals a conversion mechanism *via* nickel extrusion. Adv. Mater. **33**(44), 2101576 (2021). https://doi.org/10.1002/adma.202101576
3. R. Shao, Z. Sun, L. Wang, J. Pan, L. Yi et al., Resolving the origins of superior cycling performance of antimony anode in sodium-ion batteries: a comparison with lithium-ion batteries. Angew. Chem. Int. Ed. **63**(11), e202320183 (2024). https://doi.org/10.1002/anie.202320183
4. T. Perveen, M. Siddiq, N. Shahzad, R. Ihsan, A. Ahmad et al., Prospects in anode materials for sodium ion batteries—a review. Renew. Sustain. Energy Rev. **119**, 109549 (2020). https://doi.org/10.1016/j.rser.2019.109549
5. F. Wang, Z. Jiang, Y. Zhang, Y. Zhang, J. Li et al., Revitalizing sodium-ion batteries *via* controllable microstructures and advanced electrolytes for hard carbon. eScience **4**(3), 100181 (2024). https://doi.org/10.1016/j.esci.2023.100181
6. D.T. Pham, T.T. Vu, S. Kim, B. Sambandam, V. Mathew et al., A versatile pyramidal hauerite anode in congeniality diglyme-based electrolytes for boosting performance of Li- and Na-ion batteries. Adv. Energy Mater. **9**(37), 1900710 (2019). https://doi.org/10.1002/aenm.201900710
7. S. Li, J. Chen, J. Xiong, X. Gong, J. Ciou et al., Encapsulation of MnS nanocrystals into N, S-co-doped carbon as anode material for full cell sodium-ion capacitors. Nano-Micro Lett. **12**(1), 34 (2020). https://doi.org/10.1007/s40820-020-0367-9
8. Y. Ma, Y. Ma, G.-T. Kim, T. Diemant, R.J. Behm et al., Superior lithium storage capacity of α-MnS nanoparticles embedded in S-doped carbonaceous mesoporous frameworks. Adv. Energy Mater. **9**(43), 1902077 (2019). https://doi.org/10.1002/aenm.201902077
9. D.-H. Liu, W.-H. Li, Y.-P. Zheng, Z. Cui, X. Yan et al., *In situ* encapsulating α-MnS into N, S-codoped nanotube-like carbon as advanced anode material: α → β phase transition promoted cycling stability and superior Li/Na-storage performance in half/full cells. Adv. Mater. **30**(21), e1706317 (2018). https://doi.org/10.1002/adma.201706317
10. W. Zhao, X. Ma, L. Gao, X. Wang, Y. Luo et al., Hierarchical architecture engineering of branch-leaf-shaped cobalt phosphosulfide quantum dots: enabling multi-dimensional ion-transport channels for high-efficiency sodium storage.

Adv. Mater. **36**(4), 2305190 (2024). https://doi.org/10.1002/adma.202305190

11. Y. Zhou, M. Zhang, Q. Wang, J. Yang, X. Luo et al., Pseudocapacitance boosted N-doped carbon coated Fe7S8 nanoaggregates as promising anode materials for lithium and sodium storage. Nano Res. **13**(3), 691–700 (2020). https://doi.org/10.1007/s12274-020-2677-0
12. M. Han, J. Liu, C. Deng, J. Guo, Y. Mu et al., Yolk-shell structure and spin-polarized surface capacitance enable FeS stable and fast ion transport in sodium-ion batteries. Adv. Energy Mater. **14**(22), 2400246 (2024). https://doi.org/10.1002/aenm.202400246
13. Z. Li, G. Zhou, S. Li, H. Liu, L. Wang et al., Unlocking cycling longevity in micro-sized conversion-type FeS_2 cathodes. Joule **7**(11), 2609–2621 (2023). https://doi.org/10.1016/j.joule.2023.10.003
14. R. Hu, H. Zhao, J. Zhang, Q. Liang, Y. Wang et al., Scalable synthesis of a foam-like FeS_2 nanostructure by a solution combustion–sulfurization process for high-capacity sodium-ion batteries. Nanoscale **11**(1), 178–184 (2019). https://doi.org/10.1039/C8NR06675B
15. W. Huang, H. Sun, H. Shangguan, X. Cao, X. Xiao et al., Three-dimensional iron sulfide-carbon interlocked graphene composites for high-performance sodium-ion storage. Nanoscale **10**(16), 7851–7859 (2018). https://doi.org/10.1039/c8nr00034d
16. F. Chen, D. Shi, M. Yang, H. Jiang, Y. Shao et al., Novel designed MnS–MoS_2 heterostructure for fast and stable Li/Na storage: insights into the advanced mechanism attributed to phase engineering. Adv. Funct. Mater. **31**(6), 2007132 (2021). https://doi.org/10.1002/adfm.202007132
17. R. Liu, L. Yu, X. He, H. Liu, X. Ma et al., Constructing heterointerface of Bi/Bi_2S_3 with built-in electric field realizes superior sodium-ion storage capability. eScience **3**(4), 100138 (2023). https://doi.org/10.1016/j.esci.2023.100138
18. J. Lv, D. Bai, L. Yang, Y. Guo, H. Yan et al., Bimetallic sulfide nanoparticles confined by dual-carbon nanostructures as anodes for lithium-/ sodium-ion batteries. Chem. Commun. **54**(64), 8909–8912 (2018). https://doi.org/10.1039/C8CC04318C
19. H. Lei, H. Wang, B. Cheng, F. Zhang, X. Liu et al., Anion-vacancy modified WSSe nanosheets on 3D cross-networked porous carbon skeleton for non-aqueous sodium-based dual-ion storage. Small **19**(10), 2206340 (2023). https://doi.org/10.1002/smLl.202206340
20. Y. Liu, X. Hu, J. Li, G. Zhong, J. Yuan et al., Carbon-coated $MoS_{1.5}Te_{0.5}$ nanocables for efficient sodium-ion storage in non-aqueous dual-ion batteries. Nat. Commun. **13**(1), 663 (2022). https://doi.org/10.1038/s41467-022-28176-0
21. Z. Tian, W. Sun, J. Yu, J. Yuan, J. Chen et al., Vacancy-rich ternary iron phosphoselenide multicavity nanorods: a highly reversible and fast anode for sodium-ion batteries. Adv. Funct. Mater. **34**(39), 2404320 (2024). https://doi.org/10.1002/adfm.202404320
22. S. Xing, J. Yang, M. Muska, H. Li, Q. Yang, Rock-salt $MnS_{0.5}Se_{0.5}$ nanocubes assembled on N-doped graphene forming van der waals heterostructured hybrids as high-performance anode for lithium- and sodium-ion batteries. ACS Appl. Mater. Interfaces **13**(19), 22608–22620 (2021). https://doi.org/10.1021/acsami.1c04776
23. B. Haruna, L. Wang, X. Hu, G. Luo, M.A. Muhammad et al., Se-rich functionalized FeS_x hollow nanospheres for accelerated and long-lasting sodium storage. Adv. Funct. Mater. **35**(4), 2414246 (2025). https://doi.org/10.1002/adfm.202414246
24. B. Liu, Y. Liu, X. Hu, G. Zhong, J. Li et al., N-doped carbon modifying MoSSe nanosheets on hollow cubic carbon for high-performance anodes of sodium-based dual-ion batteries. Adv. Funct. Mater. **31**(31), 2101066 (2021). https://doi.org/10.1002/adfm.202101066
25. Y. Huang, Z. Wang, M. Guan, F. Wu, R. Chen, Toward rapid-charging sodium-ion batteries using hybrid-phase molybdenum sulfide selenide-based anodes. Adv. Mater. **32**(40), e2003534 (2020). https://doi.org/10.1002/adma.202003534
26. T. He, W. Zhao, J. Hu, C. Deng, D. Yan et al., Unveiling the double-edged behavior of controlled selenium substitution in cobalt sulfide for balanced Na-storage capacity and rate capability. Adv. Funct. Mater. **34**(8), 2310256 (2024). https://doi.org/10.1002/adfm.202310256
27. X. Hu, M. Qiu, Y. Liu, J. Yuan, J. Chen et al., Interface and structure engineering of tin-based chalcogenide anodes for durable and fast-charging sodium ion batteries. Adv. Energy Mater. **12**(47), 2202318 (2022). https://doi.org/10.1002/aenm.202202318
28. J. Zhang, Y. Wang, M. Yu, J. Ni, L. Li, Understanding the role of topotactic anion exchange in the robust Cu ion storage of $CuS_{1-x}Se_x$. ACS Energy Lett. **7**(5), 1835–1841 (2022). https://doi.org/10.1021/acsenergylett.2c00766
29. X. Wang, D. Chen, Z. Yang, X. Zhang, C. Wang et al., Novel metal chalcogenide SnSSe as a high-capacity anode for sodium-ion batteries. Adv. Mater. **28**(39), 8645–8650 (2016). https://doi.org/10.1002/adma.201603219
30. X. Wu, M. Caol, H. Lü, X. He, C. Hu, Microemulsion-mediated solvothermal synthesis and morphological evolution of $MnCO_3$ nanocrystals. J. Nanosci. Nanotechnol. **6**(7), 2123–2128 (2006). https://doi.org/10.1166/jnn.2006.371
31. J. Zhu, P. Wei, Q. Zeng, G. Wang, K. Wu et al., MnS@N, S Co-doped carbon core/shell nanocubes: sulfur-bridged bonds enhanced Na-storage properties revealed by in situ Raman spectroscopy and transmission electron microscopy. Small **16**(45), 2003001 (2020). https://doi.org/10.1002/smLl.202003001
32. C. Guo, R. Zhou, X. Liu, R. Tang, W. Xi et al., Activating the $MnS_{0.5}Se_{0.5}$ microspheres as high-performance cathode materials for aqueous zinc-ion batteries: insight into in situ electrooxidation behavior and energy storage mechanisms. Small **20**(15), 2306237 (2024). https://doi.org/10.1002/smLl.202306237
33. K.Y. Yasoda, M. Afshan, S.C. Caroline, E.M. Harini, K. Ghosh et al., Polyaniline with manganese based mixed chalcogenides (MnSSe-HT-PANI) heterostructure for the

 https://doi.org/10.1007/s40820-025-01767-4

development of high-performance flexible supercapacitor. Electrochim. Acta **480**, 143879 (2024). https://doi.org/10.1016/j.electacta.2024.143879

34. A. Zhang, R. Zhao, Y. Wang, J. Yang, C. Wu et al., Regulating the electronic structure of manganese-based materials to optimize the performance of zinc-ion batteries. Energy Environ. Sci. **16**(8), 3240–3301 (2023). https://doi.org/10.1039/D3EE01344H
35. C. Freysoldt, B. Grabowski, T. Hickel, J. Neugebauer, G. Kresse et al., First-principles calculations for point defects in solids. Rev. Mod. Phys. **86**(1), 253–305 (2014). https://doi.org/10.1103/revmodphys.86.253
36. D. Lan, Y. Zhao, Y. Liu, N. Zhu, J. Cui, Self-assembled nano-MnS@N, P dual-doped lignite based carbon as high-performance sodium-ion batteries anode. J. Energy Storage **90**, 111827 (2024). https://doi.org/10.1016/j.est.2024.111827
37. X. Xu, S. Ji, M. Gu, J. Liu, *In situ* synthesis of MnS hollow microspheres on reduced graphene oxide sheets as high-capacity and long-life anodes for Li- and Na-ion batteries. ACS Appl. Mater. Interfaces **7**(37), 20957–20964 (2015). https://doi.org/10.1021/acsami.5b06590
38. T. Wang, L. Yin, R. Zhao, C. Xia, X. Zhao et al., First-principles study of monolayer $SnS_{2(1-x)}Se_{2x}$ alloys as anode materials for lithium ion batteries. Appl. Surf. Sci. **457**, 256–263 (2018). https://doi.org/10.1016/j.apsusc.2018.06.030
39. Y. Xiao, J.-Y. Hwang, I. Belharouak, Y.-K. Sun, Superior Li/Na-storage capability of a carbon-free hierarchical CoSx hollow nanostructure. Nano Energy **32**, 320–328 (2017). https://doi.org/10.1016/j.nanoen.2016.12.053
40. T. Li, Y. Wang, L. Yuan, Q. Zhou, S. Qiao et al., An α-MnSe nanorod as anode for superior potassium-ion storage via synergistic effects of physical encapsulation and chemical bonding. Chem. Eng. J. **446**, 137152 (2022). https://doi.org/10.1016/j.cej.2022.137152
41. Y. Chu, L. Guo, B. Xi, Z. Feng, F. Wu et al., Embedding $MnO@Mn_3O_4$ nanoparticles in an N-doped-carbon framework derived from Mn-organic clusters for efficient lithium storage. Adv. Mater. **30**(6), 1704244 (2018). https://doi.org/10.1002/adma.201704244
42. C. An, Y. Yuan, B. Zhang, L. Tang, B. Xiao et al., Graphene wrapped $FeSe_2$ nano-microspheres with high pseudocapacitive contribution for enhanced Na-ion storage. Adv. Energy Mater. **9**(18), 1900356 (2019). https://doi.org/10.1002/aenm.201900356
43. W. Chen, X. Zhang, L. Mi, C. Liu, J. Zhang et al., High-performance flexible freestanding anode with hierarchical 3D carbon-networks/Fe_7S_8/graphene for applicable sodium-ion batteries. Adv. Mater. **31**(8), 1806664 (2019). https://doi.org/10.1002/adma.201806664
44. P. Ge, H. Hou, S. Li, L. Yang, X. Ji, Tailoring rod-like $FeSe_2$ coated with nitrogen-doped carbon for high-performance sodium storage. Adv. Funct. Mater. **28**(30), 1801765 (2018). https://doi.org/10.1002/adfm.201801765
45. Y. Xiao, Y. Miao, S. Hu, F. Gong, Q. Yu et al., Structural stability boosted in 3D carbon-free iron selenide through engineering heterointerfaces with Se–P bonds for appealing Na+-storage. Adv. Funct. Mater. **33**(5), 2210042 (2023). https://doi.org/10.1002/adfm.202210042
46. D.-H. Liu, W.-H. Li, H.-J. Liang, H.-Y. Lü, J.-Z. Guo et al., Coaxial α-MnSe@N-doped carbon double nanotubes as superior anode materials in Li/Na-ion half/full batteries. J. Mater. Chem. A **6**(32), 15797–15806 (2018). https://doi.org/10.1039/C8TA03967D
47. S. Cao, Q. Liu, H. Chen, H. Zhu, Y. Liu, A bimetallic induced enhanced 3D electron transport network supported by micro constrain area of balls-in-ball structure used for high performance sodium storage. Chem. Eng. J. **470**, 144277 (2023). https://doi.org/10.1016/j.cej.2023.144277
48. W. Sun, X. Tang, Q. Yang, Y. Xu, F. Wu et al., Coordination-induced interlinked covalent- and metal-organic-framework hybrids for enhanced lithium storage. Adv. Mater. **31**(37), e1903176 (2019). https://doi.org/10.1002/adma.201903176
49. S. Xing, J. Yang, C. Wang, J. Zhou, J. Zhang et al., Fabrication of van der waals heterostructured $FePSe_3$/carbon hybrid nanosheets for sodium storage with high performance. ACS Appl. Mater. Interfaces **12**(49), 54732–54741 (2020). https://doi.org/10.1021/acsami.0c16396
50. Y. Sang, L. Wang, X. Cao, G. Ding, Y. Ding et al., Emerging 2D-Layered $MnPS_3$/rGO composite as a superior anode for sodium-ion batteries. J. Alloys Compd. **831**, 154775 (2020). https://doi.org/10.1016/j.jallcom.2020.154775
51. T. Zheng, P. Hu, Z. Wang, T. Guo, 2D amorphous iron selenide sulfide nanosheets for stable and rapid sodium-ion storage. Adv. Mater. **35**(48), e2306577 (2023). https://doi.org/10.1002/adma.202306577
52. C. Wang, B. Zhang, H. Xia, L. Cao, B. Luo et al., Composition and architecture design of double-shelled $Co_{0.85}Se_{1-x}S_x$@Carbon/graphene hollow polyhedron with superior alkali (Li, Na, K)-ion storage. Small **16**(17), 1905853 (2020). https://doi.org/10.1002/smLl.201905853
53. J. Wang, J. Liu, R.T. Subramaniam, D. Zhang, Z. Li et al., Construction of $WSSe_2$/C anode with enlarged layer spacing for efficient Na^+ storage by anion synergistic strategy. J. Power. Sources **614**, 234991 (2024). https://doi.org/10.1016/j.jpowsour.2024.234991
54. S. Huang, M. Ye, Y. Zhang, Y. Tang, X. Liu et al., Achieving ultrahigh-rate and low-temperature sodium storage of $FePS_3$ via in situ construction of graphitized porous N-doped carbon. ACS Appl. Mater. Interfaces **14**(37), 42048–42056 (2022). https://doi.org/10.1021/acsami.2c10953
55. W. Brehm, A.L. Santhosha, Z. Zhang, C. Neumann, A. Turchanin et al., Copper thiophosphate (Cu_3PS_4) as electrode for sodium-ion batteries with ether electrolyte. Adv. Funct. Mater. **30**(19), 1910583 (2020). https://doi.org/10.1002/adfm.201910583
56. L. Cao, S. Fang, B. Xu, B. Zhang, C. Wang et al., Enabling reversible reaction by uniform distribution of heterogeneous intermediates on defect-rich SnSSe/C layered heterostructure for ultralong-cycling sodium storage. Small **18**(26), 2202134 (2022). https://doi.org/10.1002/smLl.202202134

57. Y.X. Chen, Y.H. Lin, Y.F. Yuan, W. Lv, M. Zhu et al., Ternary CoPSe *in situ* grown in cubic hollow carbon nanobox achieves high-rate and long-life lithium/sodium storage. Mater. Res. Bull. **167**, 112437 (2023). https://doi.org/10.1016/j.materresbull.2023.112437
58. K. Chen, G. Li, Z. Hu, Y. Wang, D. Lan et al., Construction of γ-MnS/α-MnS hetero-phase junction for high-performance sodium-ion batteries. Chem. Eng. J. **435**, 135149 (2022). https://doi.org/10.1016/j.cej.2022.135149
59. N. Zhang, X. Li, T. Hou, J. Guo, A. Fan et al., MnS hollow microspheres combined with carbon nanotubes for enhanced performance sodium-ion battery anode. Chin. Chem. Lett. **31**(5), 1221–1225 (2020). https://doi.org/10.1016/j.cclet.2019.09.050
60. G. Li, K. Chen, Y. Wang, Z. Wang, X. Chen et al., Cream roll-inspired advanced MnS/C composite for sodium-ion batteries: encapsulating MnS cream into hollow N, S-co-doped carbon rolls. Nanoscale **12**(15), 8493–8501 (2020). https://doi.org/10.1039/D0NR00626B
61. J.-S. Park, A. Lee, G.D. Park, Y.C. Kang, Synthesis of MnSe@C yolk-shell nanospheres via a water vapor-assisted strategy for use as anode in sodium-ion batteries. Int. J. Energy Res. **46**(3), 2500–2511 (2022). https://doi.org/10.1002/er.7323
62. L. Hu, L. He, X. Wang, C. Shang, G. Zhou, MnSe embedded in carbon nanofibers as advanced anode material for sodium ion batteries. Nanotechnology **31**(33), 335402 (2020). https://doi.org/10.1088/1361-6528/ab8e78
63. S. Chong, T. Li, S. Qiao, Y.-C. Yang, Z. Liu et al., Boosting manganese selenide anode for superior sodium-ion storage via triggering α → β phase transition. ACS Nano **18**(4), 3801–3813 (2024). https://doi.org/10.1021/acsnano.3c12215
64. N.-J. Song, Y. Wang, C. Ma, Q. Zhang, Y. Zhao et al., Cage-like MnSe@PPyC/rGO as superior dual anode materials in Li/Na-ions storage. J. Alloys Compd. **927**, 167002 (2022). https://doi.org/10.1016/j.jallcom.2022.167002
65. M. Yousaf, Z. Wang, Y. Wang, Y. Chen, U. Ali et al., Core–shell $FeSe_2$/C nanostructures embedded in a carbon framework as a free standing anode for a sodium ion battery. Small **16**(47), 2002200 (2020). https://doi.org/10.1002/smll.202002200
66. B.-C. Chen, X. Lu, H.-Y. Zhong, P.-W. Huang, Y.-N. Wu et al., Constructing $FePSe_3$–$FeSe_2$ heterojunctions uniformly in a Ketjen black carbon matrix for superior potassium ion batteries. J. Mater. Chem. A **10**(48), 25671–25682 (2022). https://doi.org/10.1039/d2ta07426e
67. L. Hu, C. Liu, F. Zhang, H. Wang, B. Wang, Vacancy-defect ternary topological insulators Bi_2Se_2Te encapsulated in mesoporous carbon spheres for high performance sodium ion batteries and hybrid capacitors. Small **20**(33), 2311079 (2024). https://doi.org/10.1002/smll.202311079
68. X. Ren, Y. Zhao, Q. Li, F. Cheng, W. Wen et al., A novel multielement nanocomposite with ultrahigh rate capacity and durable performance for sodium-ion battery anodes. J. Mater. Chem. A **8**(23), 11598–11606 (2020). https://doi.org/10.1039/d0ta04349d
69. L. Zhang, H. Zhao, L. Dai, F. Yao, Y. Huang et al., Sacrificial template synthesis of two-dimensional few-layer $MoSe_2$ coupled with nitrogen-doped carbon sheets for high-performance sodium ion hybrid capacitors. ACS Appl. Energy Mater. **4**(12), 14735–14745 (2021). https://doi.org/10.1021/acsaem.1c03414
70. H. Zhang, B. Liu, Z. Lu, J. Hu, J. Xie et al., Sulfur-bridged bonds heightened Na-storage properties in MnS nanocubes encapsulated by S-doped carbon matrix synthesized *via* solvent-free tactics for high-performance hybrid sodium ion capacitors. Small **19**(16), 2207214 (2023). https://doi.org/10.1002/smll.202207214
71. S. Li, J. Chen, X. Gong, J. Wang, P.S. Lee, A nonpresodiate sodium-ion capacitor with high performance. Small **14**(50), e1804035 (2018). https://doi.org/10.1002/smll.201804035
72. J. Qian, Y.S. Chui, G. Li, M. Lin, C.M. Luk et al., Kinetically controlled redox behaviors of $K_{0.3}MnO_2$ electrodes for high performance sodium-ion batteries. J. Mater. Chem. A **6**(23), 10803–10812 (2018). https://doi.org/10.1039/c8ta03543a

 https://doi.org/10.1007/s40820-025-01767-4